The Dependence of Mean Climate State on Shortwave Absorption by Water Vapor 🖉

HANJUN KIM,[a] ANGELINE G. PENDERGRASS,[b,c] AND SARAH M. KANG[a]

[a] *School of Urban and Environmental Engineering, UNIST, Ulsan, South Korea*
[b] *Department of Earth and Atmospheric Sciences, Cornell University, Ithaca, New York*
[c] *National Center for Atmospheric Research, Boulder, Colorado*

ABSTRACT: State-of-the-art climate models exhibit significant spread in the climatological value of atmospheric short-wave absorption (SWA). This study investigates both the possible causes and climatic impacts of this SWA intermodel spread. The intermodel spread of global-mean SWA largely originates from the intermodel difference in water vapor short-wave absorptivity. Hence, we alter the water vapor shortwave absorptivity in the Community Earth System Model, version 1, with the Community Atmosphere Model, version 4 (CESM1-CAM4). Increasing the water vapor shortwave absorptivity leads to a reduction in global-mean precipitation and a La Niña–like cooling over the tropical Pacific. The global-mean atmospheric energy budget suggests that the precipitation is suppressed as a way to compensate for the increased SWA. The precipitation reduction is driven by the weakened surface winds, stabilized planetary boundary layer, and surface cooling. The La Niña–like cooling over the tropical Pacific is attributed to the zonal asymmetry of climatological evaporative damping efficiency and the low cloud enhancement over the eastern basin. Complementary fixed SSTs simulations suggest that the latter is more fundamental and that it primarily arises from atmospheric processes. Consistent with our experiments, the CMIP5/6 models with a higher global-mean SWA tend to produce tropical Pacific toward a more La Niña–like mean state, highlighting the possible role of water vapor shortwave absorptivity for shaping the mean-state climate patterns.

KEYWORDS: Atmospheric circulation; Climate models; Cloud forcing; Coupled models; Model errors; Parameterization; Radiation budgets; Radiative transfer; Water vapor

1. Introduction

Atmospheric constituents such as water vapor, cloud liquid water, and aerosols absorb a significant amount of incident shortwave radiation (SW). Observational estimates indicate that the atmospheric shortwave absorption (SWA) is as large as 80 W m^{-2} in the global mean, corresponding to 24% of incident insolation (Wild et al. 2015). This absorption within the atmosphere partly sets the atmospheric stability and global hydrological cycle (Kiehl et al. 1995). Despite its significance for the climate, models have difficulty in properly simulating the SWA. The recent studies show that the CMIP5 (CMIP6) historical simulations tend to underestimate the global-mean SWA by 5.6 (4.0) W m^{-2}, with a multimodel mean of 74.4 (76.0) W m^{-2} and a substantial intermodel range of 9.9 (8.9) W m^{-2} (Wild et al. 2015; Wild 2020).

The large SWA intermodel spread potentially stems from uncertainties in the SWA by water vapor and aerosols, which are the dominant factors that introduce errors in radiation parameterizations (Kim and Ramanathan 2008; Wild 2008; Pincus et al. 2015). The water vapor is presumably the main contributor since it largely constitutes the SWA under cloud-free conditions by 43 W m^{-2} (Kiehl and Trenberth 1997). Despite continuous efforts of many modeling groups in improving the parameterization of SWA by water vapor (Freidenreich and Ramaswamy 1999; Lohmann and Bennartz 2002; Collins et al. 2006; Paynter and Ramaswamy 2014), some CMIP5 models used outdated schemes (DeAngelis et al. 2015), which possibly contributed to the large SWA intermodel spread. The misrepresentation of the aerosol optical properties and the insufficient inclusion of absorbing aerosols in some climate models can further contribute to the SWA intermodel spread (Kim and Ramanathan 2008; Wild 2020).

The uncertainty of SWA among climate models has been emphasized in studies of the global hydrological cycle intensification under global warming from the perspective of global-mean atmospheric energy budget (e.g., Takahashi 2009b). Associated with the warmer atmospheric column is the increased atmospheric longwave (LW) radiative cooling, which should be compensated by other forms of energy fluxes—SWA, sensible heat flux (SHF), and latent heat flux (LHF)—in order for the atmosphere to reach a new equilibrium state. Increases in LW cooling are primarily balanced by increases in LHF, corresponding to intensified global- and annual-mean precipitation (Allen and Ingram 2002; Previdi 2010; O'Gorman et al. 2012; Fläschner et al. 2016). However, the LHF increase is partially damped by the SWA increase from atmospheric moistening. Consequently, the models with smaller SWA increases exhibit larger precipitation increases. This strong relationship between the SWA and precipitation responses suggests the need for constraining the SWA for narrowing the uncertainty in the future projections of hydrological cycle (Takahashi 2009b; DeAngelis et al. 2015; Pendergrass 2020).

The SWA uncertainty has mostly been addressed in the context of global-mean future projections. Despite the large intermodel spread of the climatological SWA, its effect on the mean climate state has not been discussed much in the literature. Such effect can be inferred from a limited number of studies that report updated parameterization schemes for improving the SWA underestimation problem (Arking 1996; Lohmann and Bennartz 2002; Collins et al. 2006; Paynter and Ramaswamy 2014). Improved model parameterizations lead to an increase in SWA, accompanied by a reduction in global-mean precipitation. However, the global-mean SWA increases by only ~1–3 W m^{-2}, which is considerably smaller than the SWA intermodel range of 10 W m^{-2} across the CMIP ensemble. The small SWA increase led by improved parameterizations suggests that more dramatic modifications are required to encompass the range of SWA intermodel spread in the mean climate state.

In this study, we set out to diagnose the causes of the intermodel spread in global-mean SWA using the preindustrial simulations of CMIP5 and CMIP6 models (Taylor et al. 2012; Eyring et al. 2016). Then, we examine the contribution of SWA intermodel spread to the mean climate state through the experiments with Community Earth System Model version 1.2.2 (CESM 1.2.2) in which the water vapor SW absorptivity is altered to reproduce the SWA intermodel spread. Mechanisms are explored by which this SWA forcing modulates the global hydrological cycle and the tropical Pacific SST pattern. Finally, we apply our experiment results to understand the intermodel spread of the CMIP preindustrial mean climate, with a focus on the tropical Pacific SST pattern.

2. Methodology

a. Modification of radiative parameterization

We employ the CESM 1.2.2 (Gent et al. 2011), with the finite-volume Community Atmosphere Model version 4 (CAM4) atmosphere (Neale et al. 2013) and Community Land Model 4 (CLM4) land (Lawrence et al. 2011) at nominal 2° horizontal resolutions and 26 vertical layers in the atmosphere. The ocean component is Parallel Ocean Program version 2 (POP2) (Smith et al. 2010) and the sea ice model is Community Ice Code version 4 (CICE4) (Hunke and Lipscomb 2008), each with nominal 1° horizontal resolutions, and with 60 vertical layers for the ocean.

In CAM4, the SWA by water vapor is parameterized with Community Atmosphere Model Radiative Transfer (CAM-RT) scheme following Collins et al. (2006). In CAM-RT, the contribution of water vapor to SWA is proportional to the water vapor optical depth (τ_{h2o}) given by $\tau_{h2o} = uk_i$, where u is the effective water vapor path, representing the mass of water vapor, k is the absorption coefficient that parameterizes the degree of SWA per unit water vapor path, and i denotes an index for seven spectral bands covering the wavenumbers between 1000 and 18 000 cm^{-1}. The parameter k that represents the water vapor SW absorptivity primarily controls the performance of parameterization.
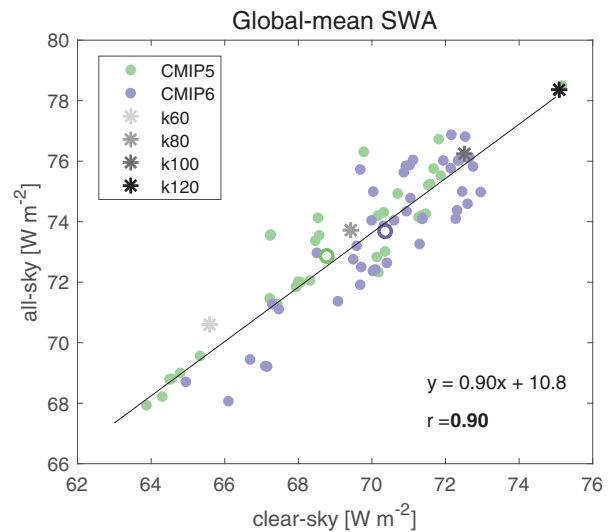

FIG. 1. Global-mean atmospheric shortwave absorption (SWA) for clear-sky and all-sky fluxes, averaged for the last 100 years of the preindustrial simulation in 34 CMIP5 (green circles) and 43 CMIP6 (blue circles) models, with the respective multimodel mean in open circles. The CMIP models used in this study are summarized in Table S1. The correlation and regression coefficients of CMIP models are inserted at the lower right corner. The correlation coefficient is statistically different from zero at the 95% confidence level using the t test. Asterisks denote the CESM FOM results with a varying water vapor shortwave absorptivity.

We alter the SWA by water vapor by multiplying the water vapor SW absorptivity (k) by the factors of 0.6, 0.8, 1.0, and 1.2 for all seven spectral bands—these experiments are respectively named k60, k80, k100, and k120. The multiplication factors are chosen in such a way that the global-mean SWA of our two extreme experiments approximately covers the range of the intermodel spread in CMIP5/6 (Fig. 1). All experiments are run with the preindustrial boundary conditions for 150 years on the fully atmosphere–ocean coupled model (which we refer to as FOM, for full ocean model). We use the last 50-yr average for the FOM analysis, when the global-mean surface temperature and net top-of-atmosphere (TOA) radiation show small temporal fluctuations (not shown). The experiments are also performed with the SSTs fixed to 1870–99 climatology of the observational dataset from Hurrell et al. (2008) (referred to as FSST), which are integrated for 30 years including the 20-yr spinup period.

b. Decomposition of the change in radiative fluxes

The variables that determine radiative fluxes in climate models include temperature, gas concentration, surface albedo, cloud, and aerosol. Soden and Held (2006) proposed a radiative kernel technique, which approximately quantifies the contribution of each climate variable to radiative flux changes. Using the CESM-CAM5 radiative kernel data from Pendergrass et al. (2018), the LW changes at TOA and surface (with the sign convention that downward is positive) are decomposed with a small error (Fig. S1 in the online
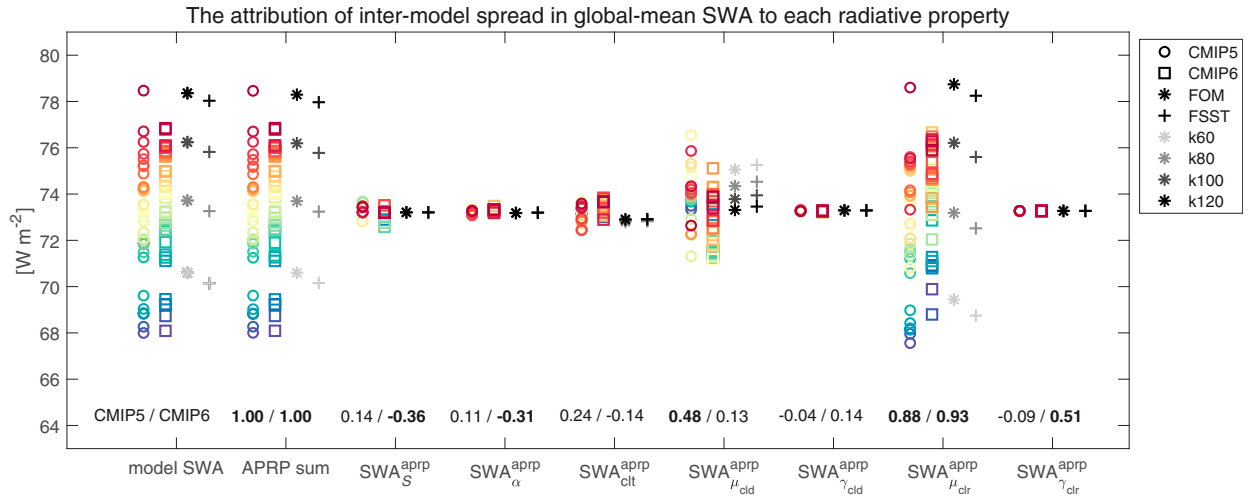
FIG. 2. The attribution of the intermodel spread of global-mean SWA to the intermodel spread in the following radiative properties: SWA_S^{aprp}, SWA_α^{aprp}, SWA_{clt}^{aprp}, $SWA_{\mu_{cld}}^{aprp}$, $SWA_{\gamma_{cld}}^{aprp}$, $SWA_{\mu_{clr}}^{aprp}$, and $SWA_{\gamma_{clr}}^{aprp}$, which respectively denote the SWA associated with the solar insolation (S), surface albedo (α), total-column cloud area fraction (clt), cloud absorptivity (μ_{cld}), cloud reflectivity (γ_{cld}), clear-sky absorptivity (μ_{clr}), and clear-sky reflectivity (γ_{clr}). The CMIP models are colored according to the global-mean SWA (circles for CMIP5 and squares for CMIP6) and the CESM FOM (asterisk) and FSST (plus sign) results are juxtaposed on the right. The multimodel mean of CMIP5/6 is treated as the reference climatology when applying the APRP method. The multimodel mean of SWA is added to the analysis. The correlation coefficients of each component to the model SWA are inserted separately for CMIP5 and CMIP6 at the bottom of the figure, with the statistically significant values at the 95% confidence level in bold.

supplemental material), following the procedure in Soden et al. (2008). By contrast, the SW changes cannot be decomposed using the radiative kernel alone in our experiments because the SW radiative parameterization is modified by the water vapor SW absorptivity. Instead, we develop an extension of the approximate partial radiative perturbation (APRP) method (Taylor et al. 2007) and combine it with the radiative kernel technique to isolate the effect of water vapor SW absorptivity.

In the APRP method, a one-layer radiation model with seven radiative properties approximates the interactions of SW fluxes within a single climate state. These seven properties are atmospheric absorption and reflection, and surface albedo, each of which is separately estimated for clear and overcast skies, and a cloud area fraction. By fitting the seven radiative properties to the total cloud area fraction and SW fluxes from standard model output, the interactions that result in SW fluxes within each climate state can be captured with reasonable accuracy. Comparison can be made between two climate states by making perturbations to radiative properties to attribute the net TOA SW responses to the various combinations of radiative property changes (see the appendix for details). APRP allows us to reasonably separate the TOA SW responses to the radiative effects of changes in surface albedo, cloud, and non-cloud atmospheric constituents, which are poorly captured with the kernel technique due to nonlinear interactions that are nonetheless straightforward in the APRP framework (Yoshimori et al. 2011; Hwang et al. 2013; Frey et al. 2017; Zelinka et al. 2020). Furthermore, it relies on variables that are commonly archived for climate model simulations.

Here, we extend the conventional APRP method focusing on atmospheric SW fluxes to the surface SW fluxes. We do this while maintaining the assumption of simultaneous atmospheric absorption and reflection at the first pass among infinite passes through a one-layer radiation model, motivated by Donohoe and Battisti (2011). We apply this assumption to the estimation of cloud radiative effects following Taylor et al. (2007):

$$\delta SW = \delta SW_\alpha^{aprp} + \delta SW_{cld}^{aprp} + \delta SW_{ncld}^{aprp}, \quad (1)$$

where δ indicates the difference between two climate states, SW indicates the shortwave flux at either TOA or surface, the superscript aprp denotes the calculation method, and the subscripts α, cld, and ncld denote, respectively, the contribution from the surface albedo, cloud, and non-cloud atmospheric constituents. The derivation for the extended APRP method is given in the appendix. We verify the skill of the modified APRP technique by comparing the SW flux change at the surface (with the sign convention that downward is positive) in response to the perturbation in SWA in our CESM experiments with the sum of the APRP components; APRP successfully reproduces the climate model (Fig. S2). Note that we not only use the APRP and radiative kernel method for the responses in one climate model, but also apply it to the intermodel spread, by setting multimodel mean as the reference climate state and individual models as target climate states.

For the differences between the experiments with altered water vapor shortwave absorptivity, a combination of the above APRP and radiative kernel methods allows us to attribute the downward positive SW flux responses to changes in

surface albedo, cloud, specific humidity (q), and the direct forcing from the altered water vapor shortwave absorptivity (k):

$$\delta\text{SW} = \delta\text{SW}^{\text{aprp}}_{\alpha} + \delta\text{SW}^{\text{aprp}}_{\text{cld}} + \delta\text{SW}^{\text{kernel}}_q + \delta\text{SW}_k, \qquad (2)$$

$$\delta\text{SW}_k = \delta\text{SW}^{\text{aprp}}_{\text{ncld}} - \delta\text{SW}^{\text{kernel}}_q, \qquad (3)$$

where the superscripts denote the calculation method. In our experiments, the SW response due to the changes in non-cloud atmospheric constituents $\delta\text{SW}^{\text{aprp}}_{\text{ncld}}$ can only result from changes in specific humidity or water vapor SW absorptivity. Hence, we obtain the forcing term δSW_k by subtracting the specific humidity contribution calculated with the radiative kernel technique $\delta\text{SW}^{\text{kernel}}_q$ from $\delta\text{SW}^{\text{aprp}}_{\text{ncld}}$ [Eq. (3)].

c. Diagnostic equation for SST changes

To understand changes in the SST pattern, the energy budget equation for ocean mixed layer is reformulated to approximately quantify the relative contributions of each surface flux component to the regional SST changes (Xie et al. 2010; Zhang and Li 2014). Assuming an equilibrium in the ocean mixed layer, the anomalous heat budget equation for the mixed layer is

$$0 = \delta\text{SW}_{\text{sfc}} + \delta\text{LW}_{\text{sfc}} - \delta\text{LHF} - \delta\text{SHF} + \delta\text{OHT}, \qquad (4)$$

where LHF is latent heat flux, SHF is sensible heat flux, and OHT is the convergence of oceanic heat transport by three-dimensional advection, which is substituted by the net upward surface heat flux following Xie et al. (2010). Using the bulk formula, LHF can be expressed as a function of surface temperature, near-surface relative humidity, near-surface atmospheric stability, and wind speed. Therefore, δLHF can be decomposed into the components due to the surface temperature change (δT_s) and others (Jia and Wu 2013), then substituted into Eq. (4):

$$0 = \delta\text{SW}_{\text{sfc}} + \delta\text{LW}_{\text{sfc}} - (\beta\overline{\text{LHF}})\delta T_s$$
$$- \delta\text{LHF}_{\text{others}} - \delta\text{SHF} + \delta\text{OHT}, \qquad (5)$$

where the overbar indicates the reference climatology and $\beta = L_v/R_v\overline{T_s^2}$, with latent heat of vaporization $L_v = 2.5 \times 10^6$ J kg^{-1} and $R_v = 461.5$ J kg^{-1} K^{-1}. The term $\delta\text{LHF}_{\text{others}}$ denotes δLHF due to factors other than surface temperature change, calculated as $\delta\text{LHF}_{\text{others}} = \delta\text{LHF} - (\partial\text{LHF}/\partial T_s)\delta T_s = \delta\text{LHF} - (\beta\overline{\text{LHF}})\delta T_s$ [see Eq. (5) in Zhang and Li (2014)]. Equation (5) then can be reformulated to a diagnostic equation for the SST changes:

$$\delta T_s = \frac{\delta\text{SW}_{\text{sfc}} + \delta\text{LW}_{\text{sfc}} - \delta\text{LHF}_{\text{others}} - \delta\text{SHF} + \delta\text{OHT}}{\beta\overline{\text{LHF}}}. \qquad (6)$$

Note that the denominator in Eq. (6) $\beta\overline{\text{LHF}} = \partial\text{LHF}/\partial T_s$ denotes the degree of LHF change in response to unit SST increase for each model grid, representing the climatological evaporative damping efficiency. This evaporative damping
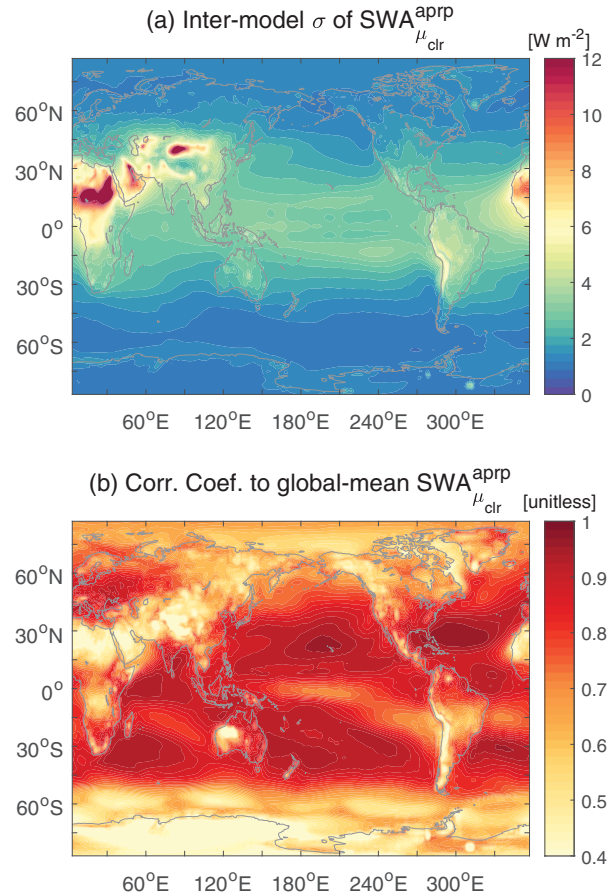
(a) Inter-model σ of SWA$^{\text{aprp}}_{\mu_{\text{clr}}}$

(b) Corr. Coef. to global-mean SWA$^{\text{aprp}}_{\mu_{\text{clr}}}$

FIG. 3. (a) The intermodel standard deviation of the SWA associated with the clear-sky absorptivity (SWA$^{\text{aprp}}_{\mu_{\text{clr}}}$). (b) The correlation coefficients between SWA$^{\text{aprp}}_{\mu_{\text{clr}}}$ at each model grid point and the global-mean SWA$^{\text{aprp}}_{\mu_{\text{clr}}}$. Both the CMIP5 and CMIP6 models are used in the analysis, but considering CMIP5/6 separately yields similar results.

efficiency is shown to dominate the spatial structure of net surface flux sensitivity to unit SST change over the tropics (Zhang and Li 2014). Hence, among various surface flux components in Eq. (4), only δLHF is expressed as function of δT_s in order to use evaporative damping efficiency as denominator in Eq. (6) while avoiding the complexity from other SST-dependent terms of $\delta\text{LW}_{\text{sfc}}$ and δSHF.

3. Results

a. Intermodel spread of SWA in CMIP

To characterize the SWA intermodel spread in the state-of-the-art climate models, we calculate the global-mean SWA for all-sky and clear-sky fluxes for the preindustrial climate in 34 CMIP5 and 43 CMIP6 models (Fig. 1), where SWA is defined as the difference between net downward SW flux at the TOA and surface. The maximum range of the spread for all-sky fluxes is 10.6 W m^{-2}. The spread originates mostly from the clear-sky component, indicated by the large

(a) Effect of the water vapor distribution

(b) Clear-sky SW absorption curve

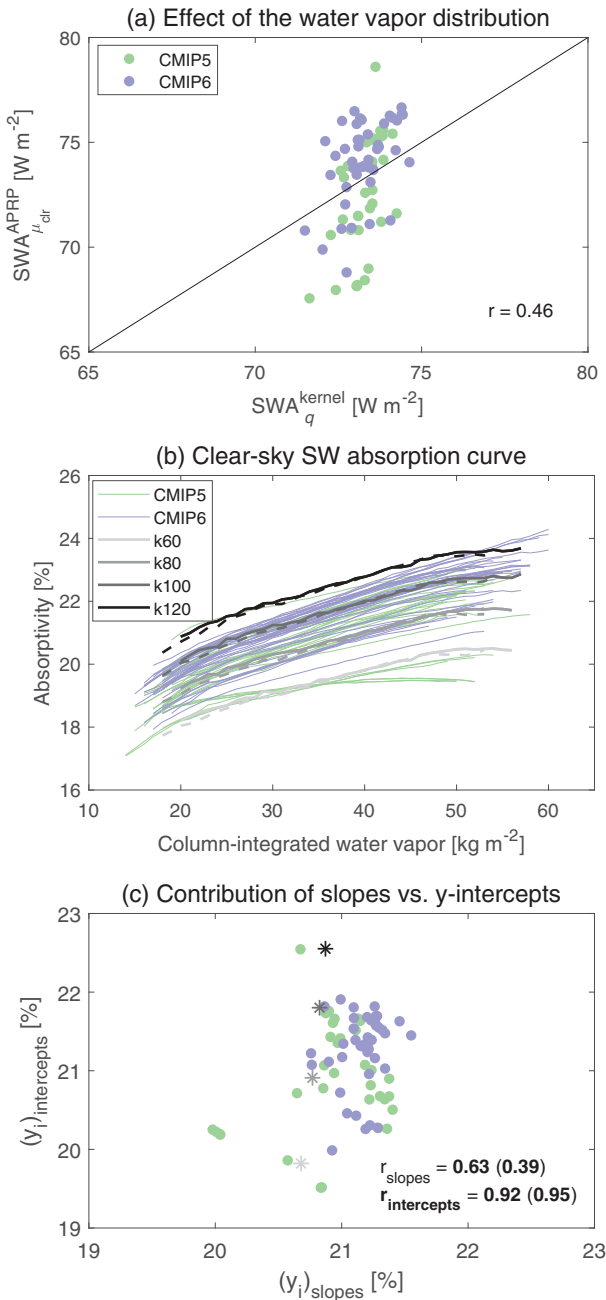(c) Contribution of slopes vs. y-intercepts

FIG. 4. (a) The scatterplot between the global-mean SWA estimated from the specific humidity radiative kernel (SWA$_q^{kernel}$) and that associated with the clear-sky absorptivity (SWA$_{\mu_{clr}}^{aprp}$). Green (blue) circles denote the CMIP5 (CMIP6) preindustrial simulations. Note that the multimodel mean of CMIP5/6 is treated as the reference climatology in the radiative kernel calculation. The multimodel mean of global-mean SWA is added in the analysis. (b) The clear-sky atmospheric SW absorptivity with respect to the column-integrated water vapor. Green (blue) solid lines indicate the CMIP5 (CMIP6) models, and the achromatic colored lines indicate the CESM experiments with FOM in solid and FSST in dashed. (c) The contribution of the intermodel spread in the linear regression slopes and y intercepts of the absorption curves to the intermodel spread of SW absorptivity at the reference water vapor amount

correlation coefficient of 0.90 and a regression coefficient close to one. We then use the APRP method to further investigate the causes of the intermodel spread in global-mean SWA (Fig. 2). The sum of all radiative components from APRP coincides well with the model SWA, indicating that this method can be used to explain the intermodel spread. The SWA intermodel spread originates mostly from the intermodel differences in the clear-sky absorptivity (SWA$_{\mu_{clr}}^{aprp}$), indicated by the high correlation and the comparable range between the model SWA and SWA$_{\mu_{clr}}^{aprp}$, for both the CMIP5 and CMIP6 ensembles.

The geographical distribution of the intermodel spread in SWA$_{\mu_{clr}}^{aprp}$ provides insight into the origin of the SWA intermodel spread (Figs. 3a,b). The clear-sky SWA occurs through atmospheric gases including water vapor, which have a relatively zonally symmetric distribution over the globe, and aerosols, with localized peaks over the deserts in northern Africa and central Asia where the aerosol optical depth is high due to natural aerosol emissions (Fiedler et al. 2019). To explore the effect of the spatial pattern of SWA on the global-mean SWA, we calculate the intermodel correlation coefficients between SWA$_{\mu_{clr}}^{aprp}$ at each grid point and its global mean (Fig. 3b). Equatorward of 60°, where most of the global-mean SWA occurs (e.g., 92.7% based on the multimodel mean of CMIP5/6 preindustrial climate), ocean regions with lower aerosol optical depth exhibit high correlation coefficients, whereas the desert regions with high natural aerosol emissions show relatively low correlations. Since the gaseous absorption dominates over the ocean but coincides with the aerosol absorption over the deserts, high correlations over the ocean indicate that the uncertainty of gaseous absorption contributes most to the intermodel spread in global-mean SWA.

The intermodel spread of gaseous SWA should largely originate from the differences in water vapor absorption, which constitutes almost 72% of the total gaseous SWA (Kiehl and Trenberth 1997). The differences can be further ascribed to 1) the water vapor distribution (the amount and the spatial pattern) and 2) radiative parameterization of the water vapor SWA (how much SW is absorbed by given amount of water vapor). First, we estimate the effect of the water vapor distribution by comparing the global-mean SWA$_{\mu_{clr}}^{aprp}$ with the global-mean SWA$_q^{kernel}$ using the same specific humidity radiative kernel for all models (Fig. 4a). Adopting the same radiative kernel excludes the contribution from differences in parameterization among models. The intermodel variance in SWA$_q^{kernel}$ is only 6.6% of that in SWA$_{\mu_{clr}}^{aprp}$, indicating that the uncertainty in parameterizations is mostly responsible for the intermodel spread of global-mean SWA.

←
w_{ref} = 37.5 kg m^{-2}. The achromatic colored asterisks indicate the CESM FOM experiments. The correlation coefficients of each contribution and the intermodel spread of global-mean SWA are inserted in the lower right corner. The values in the parentheses are the correlation coefficients excluding four outliers, CMIP5 GISS models (Table S1).
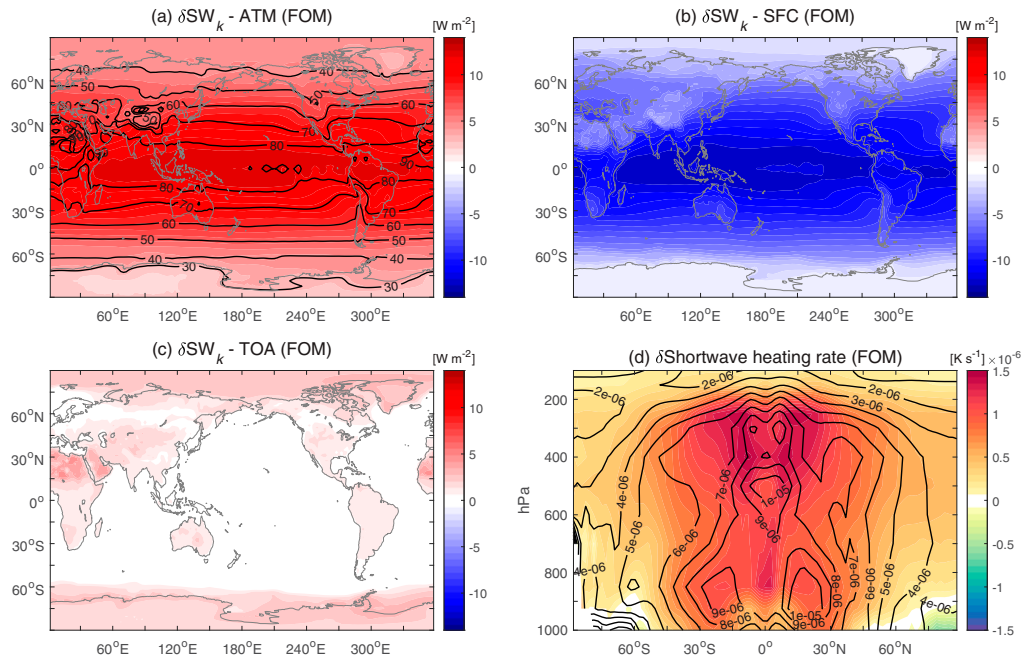
FIG. 5. The SW forcing due to the increase in water vapor SW absorptivity δSW_k (k120 − k60 in FOM) at the (a) atmospheric column, (b) surface, and (c) TOA, of which the sign conventions are inward positive in (a) and downward positive in (b) and (c). (d) The change in zonally averaged atmospheric SW heating rate. The black contours in (a) and (d) indicate the reference climatology (k60).

To evaluate the uncertainty in parameterization of SWA by water vapor among models, the clear-sky absorptivity—clear-sky SWA divided by solar insolation—at each grid point over the tropical ocean (30°S–30°N) is averaged after sorting into corresponding bins of column-integrated water vapor amount, providing the absorption curve for each model as in DeAngelis et al. (2015) (Fig. 4b). To distinguish the contribution of intermodel differences in the slopes and y intercepts in driving the intermodel differences in the absorption curve, we calculate the linear regression line for each model: $y_i = a_i w + b_i$, where a_i and b_i indicate the best-fit slope and the y intercept for each model i within the range of column-integrated water vapor amount w. The contribution of different slopes to the absorption curves is estimated as $(y_i)_{slopes} = a_i w_{ref} + \overline{b}$, by using the reference water vapor amount $w_{ref} = 37.5$ kg m^{-2}, and the multimodel mean intercept $\overline{b}$ with the slope for each model a_i. Similarly, the contribution of different intercepts is estimated as $(y_i)_{intercepts} = \overline{a} w_{ref} + b_i$ with the multimodel mean slope $\overline{a}$ and the y intercept for each model b_i. Figure 4c indicates that the differences in absorption curves mostly originate from a large range of y intercepts, rather than slopes. This means that a different degree of absorptivity for the given amount of water vapor across models contributes most to the intermodel spread of global-mean SWA climatology. The absorptivity for a given amount of water vapor is higher in CMIP6 than CMIP5 on average, which explains the partial increase in global-mean SWA from CMIP5 to CMIP6 (Fig. 1). Note that differences in the slope of absorption curves—different degrees of absorptivity enhancement per unit

water vapor increase—are important for explaining the intermodel uncertainty in SWA enhancement with global warming (DeAngelis et al. 2015). This implies that different aspects of water vapor SWA parameterization matter for the uncertainty in future projections compared to the mean climate state.

This leads us to ask, what is the impact of the SWA intermodel spread on mean climate state? We address this question by altering the water vapor SW absorptivity in CESM, as described in section 2a. The experiments capture the intermodel spread in the intercepts of the absorption curves while retaining a similar slope, roughly consistent with the behavior of the CMIP models (Fig. 4b). We next examine the effects of varying water vapor SW absorptivity on a wide range of climate patterns, including the SST, precipitation, and large-scale atmospheric circulation.

b. Overarching response in water vapor SW absorptivity experiments

To understand the effect of the increased water vapor SW absorptivity, the results from the lowest absorptivity (k60) are subtracted from the highest case (k120). Because the climate responses are generally linear to the degree of absorptivity enhancement, the results shown for k120 − k60 are similar to those for k100 − k60 and k80 − k60.

First, the direct effects of the increased absorptivity on the SW fluxes (δSW_k) are calculated following Eq. (3), which we consider to be the forcing on the climate system (Fig. 5). The
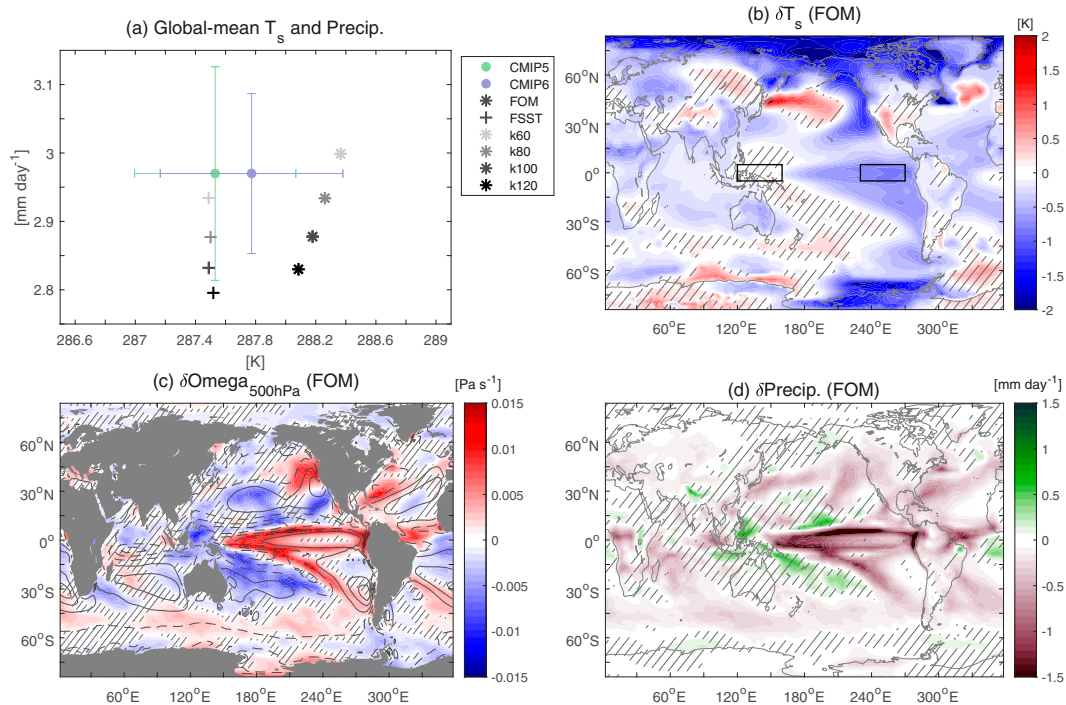
FIG. 6. (a) Global-mean surface temperature and precipitation in the CESM experiments with varying water vapor SW absorptivity (gray to black symbols) in FOM (asterisk) and FSST (plus sign) configurations. The multimodel mean value of the CMIP5 (CMIP6) preindustrial climate is denoted as a green (blue) circle, with the error bars indicating the one intermodel standard deviation. The difference between k120 and k60 in (b) surface temperature, (c) 500-hPa pressure velocity, and (d) precipitation due to the increased water vapor SW absorptivity in FOM. The contour in (c) indicates the reference climatology (k60), with the descending motion in solid and ascending motion in dashed (interval = 2×10^{-2} Pa s^{-1}). The regions are hatched where the change is not statistically different from zero at the 95% confidence level using a t test.

atmospheric forcing follows the climatological profile since the water vapor SW absorptivity is increased in the same proportion globally, yielding a zonally uniform structure with a maximum value near the equator (Fig. 5a). As the SW radiation is absorbed by the atmosphere before reaching the surface, the increased absorptivity causes a reduction of net downward SW radiation at the surface (Fig. 5b). Similarly, as the SW radiation is absorbed before being reflected by the surface back to the TOA, the net downward TOA SW radiation increases, most notably over the regions with high surface albedo (Fig. 5c). However, when averaged over the globe, the SW forcing at TOA is considerably smaller than within the atmospheric column or at the surface.

As a result of the reduced SW radiation at the surface, the global-mean surface temperature decreases (Fig. 6a). The difference in the global-mean surface temperature among the FOM experiments reaches −0.28 K, which is less than half of the intermodel standard deviation of 0.63 K in the CMIP5/6 preindustrial simulations. By contrast, the increased SW absorption within the atmosphere leads to a large reduction in the global-mean precipitation as much as 0.17 mm day^{-1}. Even without any SST changes in FSST, the global-mean precipitation is reduced by up to 0.14 mm day^{-1}, comparable to the intermodel standard deviation across the CMIP5/6

ensemble. This is also comparable to the degree of precipitation intensification due to CO_2 doubling (Fläschner et al. 2016). The detailed mechanism for the precipitation response is investigated in sections 3c and 3d.

Despite a largely zonally uniform SW surface forcing over the ocean (Fig. 5b), the increased water vapor SW absorptivity features a clear La Niña–like cooling in the tropical Pacific, with the most pronounced cooling in the eastern basin (Fig. 6b). The resultant increase in zonal SST gradient across the tropical Pacific leads to a strengthening and westward extension of the Walker circulation (Fig. 6c), causing a drier equatorial Pacific (Fig. 6d). The feedbacks responsible for such zonal asymmetry will be examined in section 3e.

The vertical structure of the forcing, inferred from the change in the shortwave heating rate, shows a stronger heating in the upper than the lower troposphere (Fig. 5d). Associated with this enhanced atmospheric stability, the Hadley circulation weakens, even in the absence of SST changes (Fig. 7b). The Hadley circulation weakening is amplified in FOM (Fig. 7a) as the tropical SSTs are allowed to drop (Fig. 6b). In addition, the Hadley circulation expands poleward (Figs. 7a,b) associated with an increase in the static stability of the subtropics (Fig. 5d), which shifts the latitude of baroclinic instability onset poleward (Lu et al. 2007).
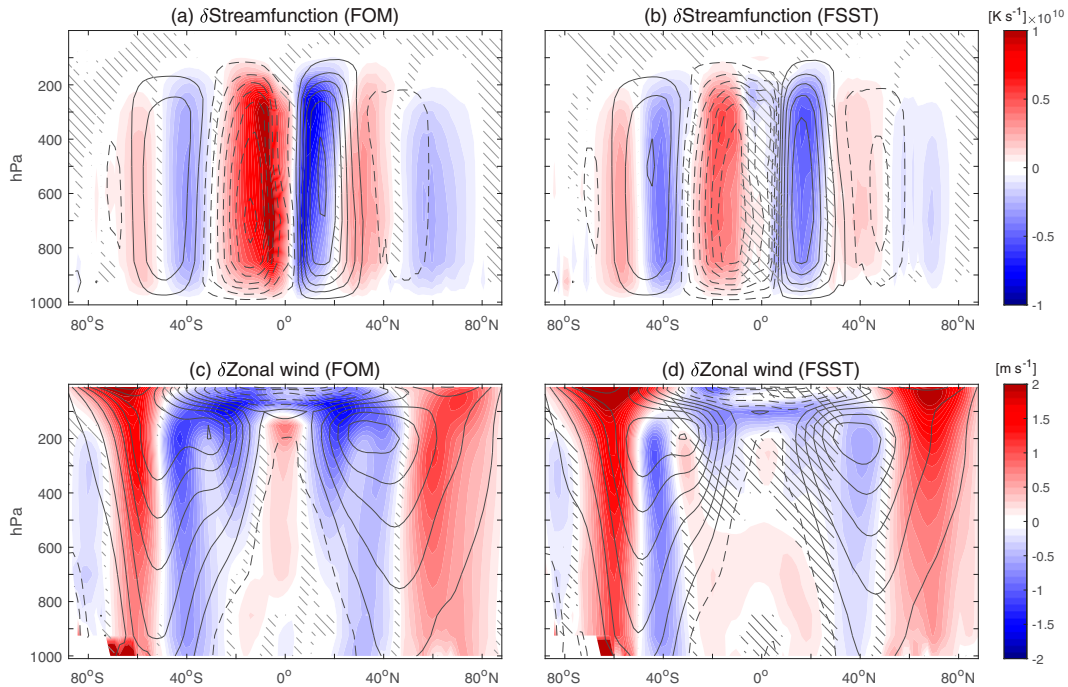
FIG. 7. (a),(b) The difference between k120 and k60 in mean meridional mass streamfunction in shading, with the reference climatology (k60) in contours. Solid denotes the clockwise circulation, and dashed denotes the counterclockwise circulation (interval = 15×10^9 kg s^{-1}). (c),(d) As in (a) and (b), but for the zonally averaged zonal wind. Solid denotes westerlies, and dashed denotes easterlies (interval = 5 m s^{-1}). Results are for FOM in (a) and (c) and FSST in (b) and (d). The regions are hatched where the change is statistically insignificant at the 95% confidence level using a t test.

Consequently, the midlatitude barotropic jet shifts poleward even without any SST changes (Figs. 7c,d).

c. Energy budget response in SWA experiments

As stated in section 1, the change in global-mean LHF is constrained by the change in atmospheric radiative cooling and SHF. Thus, one can explain a change in global-mean precipitation by examining the change in atmospheric energy budget. Figure 8a compares the global-mean changes in atmospheric energy budget: the SW forcing component (δSWA_k), the SWA change due to the radiative feedbacks (δSWA_{fdbck}), the change in longwave absorption within the atmosphere (δLWA), the change in sensible heat flux (δSHF), and the change in latent heat flux (δLHF). Following Eq. (2), δSWA_{fdbck} is separated into the contribution from changes in cloud (δSWA_{cld}^{aprp}), specific humidity (δSWA_q^{kernel}), and surface albedo (δSWA_α^{aprp}) as shown in Fig. 8b. Similarly, δLWA is attributed to the changes in atmospheric and surface temperature ($\delta LWA_{temp}^{kernel}$), cloud ($\delta LWA_{cld}^{kernel}$), and specific humidity (δLWA_q^{kernel}) as shown in Fig. 8c. The detailed decompositions allow us to explain how the atmospheric energy components adjust to the atmospheric stabilization from increased SW forcing (Fig. 5d).

The enhanced water vapor SW absorptivity produces δSWA_k by 9.33 W m^{-2} (9.26 W m^{-2}) in FOM (FSST) (Fig. 8a). This forcing is partly offset by δSWA_{fdbck}, which

mainly occurs through δSWA_{cld}^{aprp} that compensates 16.8% (14.8%) of the forcing in FOM (FSST) (Fig. 8b). The SWA_{cld}^{aprp} decreases because the increased absorption by water vapor depletes the SW flux that would otherwise be absorbed by cloud water, due to an overlap between the absorption bands of water vapor and cloud water. Both δSWA_q^{kernel} and δSWA_α^{aprp} are small for both FOM and FSST (Fig. 8b).

The δLWA compensates a further 19.9% (29.3%) of the forcing in FOM (FSST) (Fig. 8a). Decomposition of δLWA indicates that both $\delta LWA_{temp}^{kernel}$ and $\delta LWA_{cld}^{kernel}$ are responsible for the compensation (Fig. 8c). A reduced $\delta LWA_{temp}^{kernel}$ in FSST is associated with the tropospheric temperature increase (Fig. 9b), which enhances the LW emission toward the TOA and surface. The $\delta LWA_{temp}^{kernel}$ compensation is weaker with the SST adjustments in FOM (Fig. 8c) because of the temperature reduction in the lower troposphere following the SST cooling (Fig. 9a). By contrast, a reduced $\delta LWA_{cld}^{kernel}$ (Fig. 8c) is associated with not only the cloud water reduction in the upper troposphere (Figs. 9c,d), which decreases the positive LW cloud radiative effect at TOA, but also the cloud water increase in the lower troposphere, which enhances the LW emission to the surface. The resulting LW changes both at the TOA and surface hence contribute to negative $\delta LWA_{cld}^{kernel}$. The downward shift of cloud water from the upper to lower troposphere occurs as the increased water vapor SW absorptivity suppresses the
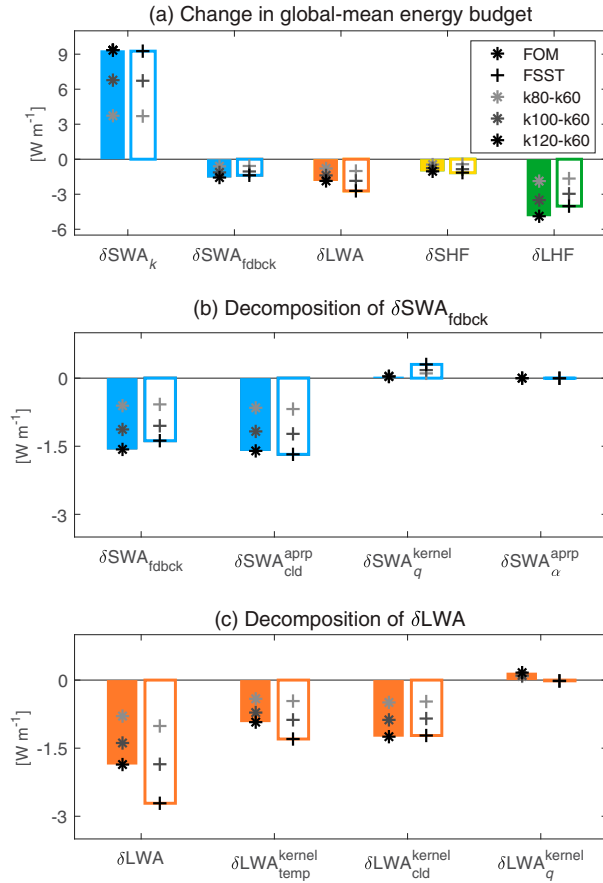
FIG. 8. (a) The change in global-mean energy budget due to the water vapor SW absorptivity increase. (b) The decomposition of $\delta\text{SWA}_{\text{fdbck}}$ into the change due to the cloud ($\delta\text{SWA}_{\text{cld}}^{\text{aprp}}$), specific humidity ($\delta\text{SWA}_q^{\text{kernel}}$) and surface albedo ($\delta\text{SWA}_\alpha^{\text{aprp}}$). (c) The decomposition of δLWA into the change due to the surface and atmospheric temperature ($\delta\text{LWA}_{\text{temp}}^{\text{kernel}}$), cloud ($\delta\text{LWA}_{\text{cld}}^{\text{kernel}}$), and specific humidity ($\delta\text{LWA}_q^{\text{kernel}}$). Asterisks indicate FOM results and plus symbols indicate FSST results, with the bars indicating the largest response k120 − k60 for reference (closed bar for FOM and open bar for FSST).

convection, trapping the moisture within the lower troposphere, leading to a relative humidity reduction in the upper and increase in the lower troposphere (not shown). Changes in specific humidity (Figs. 9e,f) have little impact on $\delta\text{LWA}_q^{\text{kernel}}$ (Fig. 8c) because the specific humidity above 700 hPa causes atmospheric LW heating while the specific humidity below 700 hPa causes atmospheric LW cooling, according to the specific humidity radiative kernel (Pendergrass et al. 2018).

Of the forced SW change, δSWA_k, 12.4% (11.9%) is compensated by δSHF in FOM (FSST) (Fig. 8a), resulting from increased near-surface stability (not shown). The remaining forcing is compensated by δLHF, which commands 52.4% (43.4%) of the total compensation (Fig. 8a). We now proceed to understand the atmospheric processes that drive the evaporation reduction (equivalent to

precipitation reduction) by performing an attribution analysis using the bulk formula.

d. Mechanism of evaporation reduction

The reduction in evaporation mostly occurs over the ocean ($\delta\text{LHF}_{\text{OCN}}$), with a minor contribution from the land ($\delta\text{LHF}_{\text{LND}}$) (Fig. 10). Since the evaporation over the ocean is parameterized through a bulk formula assuming a saturated surface, $\delta\text{LHF}_{\text{OCN}}$ can be decomposed into components due to the change in surface wind speed ($\delta\text{LHF}_{\text{WND}}$), relative humidity at model reference level ($\delta\text{LHF}_{\text{RH}}$), near-surface atmospheric stability ($\delta\text{LHF}_{\Delta T}$), and surface temperature δLHF_{T_s} following Jia and Wu (2013):

$$\delta\text{LHF}_{\text{OCN}} = \left(\frac{\overline{\text{LHF}}}{\overline{\text{WND}}}\right)\delta\text{WND} + \left(\frac{-\overline{\text{LHF}}}{e^{-\beta\overline{\Delta T}} - \overline{\text{RH}}}\right)\delta\text{RH}$$

$$+ \left(\frac{-\beta\overline{\text{LHF}}\,\overline{\text{RH}}}{e^{-\beta\overline{\Delta T}} - \overline{\text{RH}}}\right)\delta(\Delta T) + (\beta\overline{\text{LHF}})\delta T_\Omega$$

$$= \delta\text{LHF}_{\text{WND}} + \delta\text{LHF}_{\text{RH}} + \delta\text{LHF}_{\Delta T} + \delta\text{LHF}_{T_s}, \tag{7}$$

where the overbar indicates the reference climatology, WND the surface wind speed, RH the relative humidity at model reference level, $\Delta T = T_{\text{ref}} - T_s$ (with T_{ref} being the reference level temperature and T_s the surface temperature), and $\beta = L_v/R_v\overline{T_s^2}$ as introduced in section 2c. The similarity between the sum of all components (SUM) and the actual model response ($\delta\text{LHF}_{\text{OCN}}$) validates the applicability of this decomposition (Fig. 10 and Fig. S3).

Three of the components, $\delta\text{LHF}_{\text{WND}}$, $\delta\text{LHF}_{\text{RH}}$, and $\delta\text{LHF}_{\Delta T}$, are reduced by a comparable magnitude between FOM and FSST (Fig. 10). This implies that the atmospheric processes independent of SST changes are important for the variations in wind speed, relative humidity, and stability. We first examine $\delta\text{LHF}_{\text{WND}}$ in FSST. As discussed in section 3b, the increased atmospheric SW heating leads to a weakening of the Hadley circulation even in the absence of SST changes (Fig. 7b), reducing the surface wind convergence toward the ITCZ and subsequently LHF$_{\text{WND}}$ over the tropics equatorward of 30° (Fig. 11b). LHF$_{\text{WND}}$ is also reduced over the extratropics in association with a poleward shift of the extratropical jet (Fig. 7d), which leads to the negative $\delta\text{LHF}_{\text{WND}}$ in the midlatitudes and the positive $\delta\text{LHF}_{\text{WND}}$ at high latitudes (Fig. 11b). The midlatitude $\delta\text{LHF}_{\text{WND}}$ outweighs the high-latitude $\delta\text{LHF}_{\text{WND}}$ because LHF is more sensitive to a unit change in wind speed at lower latitudes, as the sensitivity of the LHF change is proportional to its climatological magnitude (Xie et al. 2010). As the SSTs are allowed to change in FOM, a La Niña–like cooling intensifies the surface easterlies in the central Pacific, partially offsetting the reduced $\delta\text{LHF}_{\text{WND}}$ over the tropics (cf. Figs. 11a,b). Hence, FOM yields a weaker reduction in LHF$_{\text{WND}}$ than FSST (Fig. 10).

Next, $\delta\text{LHF}_{\text{RH}}$ is strongly correlated with the changes in planetary boundary layer (PBL) height ($r = 0.81$) regardless of the SST configuration (Figs. 11c,d). Enhanced heating aloft stabilizes the atmosphere over the ocean, as discussed in
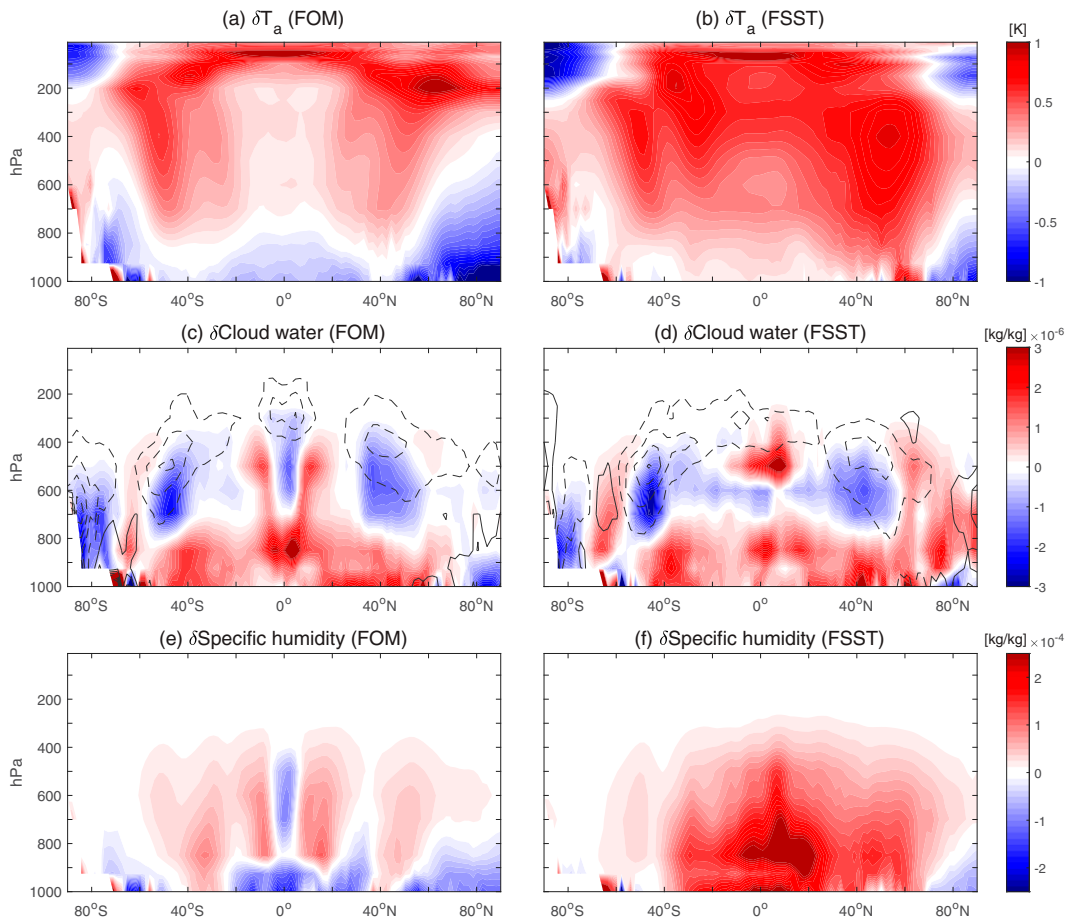
FIG. 9. The difference between k120 and k60 in zonally averaged (a) atmospheric temperature, (c) cloud liquid water (shading) and cloud ice water (contours with positive in solid and negative in dashed; interval = 2×10^{-7}), and (e) specific humidity in FOM. (b),(d),(f) As in (a), (c), and (e), but in FSST.

section 3b, resulting in a shallower PBL. The contracted PBL raises the relative humidity at the model reference level, thereby reducing LHF_{RH}. Finally, the negative $\delta\text{LHF}_{\Delta T}$ is associated with an increase in the near-surface atmospheric stability due to the larger heating in the atmosphere than at the surface, for both FOM and FSST. Thus, the evaporation is largely reduced by atmospheric processes, leaving 24.4% of reduction by δLHF_{T_s} in FOM (Fig. 10). The SST cooling decreases saturation vapor pressure at the ocean surface, amplifying the evaporation reduction in FOM compared to FSST.

Then, how does reduction of evaporation act to compensate for increased SWA aloft? The evaporation reduction near the surface curtails the moisture supply to the free atmosphere, effectively reducing the convective heating within the atmospheric column. Indeed, the atmospheric temperature tendency due to moist processes decreases significantly in the free atmosphere, compensating the increase in atmospheric SW heating most strongly among all physics terms in the atmospheric temperature tendency equation (not shown). This result indicates the strong coupling between evaporation,

convection, and atmospheric SW heating, as described by the theoretical framework in Takahashi (2009a).

e. Tropical Pacific SST pattern response in SWA experiments

In response to the increased water vapor SW absorptivity, the SST in the eastern equatorial Pacific (5°S–5°N, 230°–270°E) decreases while the SST in the western equatorial Pacific (5°S–5°N, 120°–160°E) changes little, resembling a La Niña–like cooling pattern (Fig. 6b). The eastern Pacific cooling response is significant at the 95% confidence level and is comparable to one intermodel standard deviation calculated from the CMIP5/6 preindustrial simulations (not shown). To understand the SST pattern formation, we decompose the SST changes in the western and eastern equatorial Pacific into contributions related to surface flux variations using Eq. (6) (Fig. 12). Note that only the relevant terms are shown for simplicity.

The enhanced zonal SST gradient across the equatorial Pacific arises from the SW component (δT_{SW}), while all other components act to offset the zonal asymmetry (Fig. 12a). The
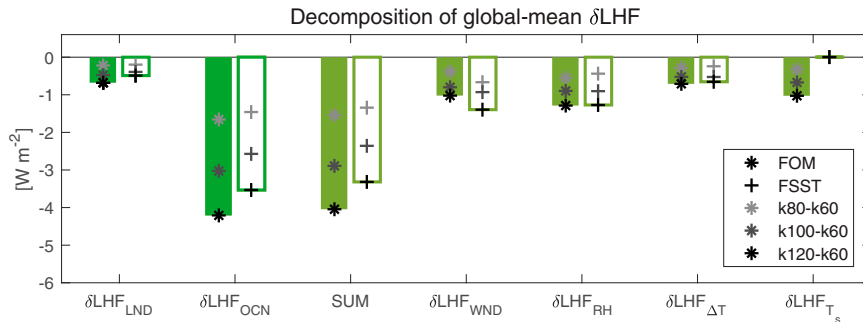
FIG. 10. Decomposition of changes in global-mean latent heat flux. Here, $\delta\mathrm{LHF_{LND}}$ ($\delta\mathrm{LHF_{OCN}}$) indicates the contribution from land (ocean) region to the global-mean change. The $\delta\mathrm{LHF_{OCN}}$ is decomposed into the change due to the surface wind speed ($\delta\mathrm{LHF_{WND}}$), relative humidity at model reference level ($\delta\mathrm{LHF_{RH}}$), near-surface stability ($\delta\mathrm{LHF_{\Delta T}}$), and surface temperature ($\delta\mathrm{LHF_{T_s}}$). The summation of all components (SUM) well matches $\delta\mathrm{LHF_{OCN}}$, justifying the use of the decomposition method [Eq. (7)].

zonal asymmetry in δT_{SW} results from both the forcing ($\delta T_{\mathrm{SW},k}$) and the SW cloud effect ($\delta T_{\mathrm{SW,cld}}$). The LW component ($\delta T_{\mathrm{LW}}$) then partially compensates the zonal gradient in δT_{SW}, mostly through the LW cloud effect ($\delta T_{\mathrm{LW,cld}}$). The zonal asymmetry is further compensated by the non-SST-related evaporation responses ($\delta T_{\mathrm{LHF,others}}$) while the effect of SHF (δT_{SHF}) is negligible. The ocean heat transport

component (δT_{OHT}) acts to compensate the strong cooling in the eastern equatorial Pacific, presumably via a weakened upwelling associated with the weaker Hadley circulation.

The surface flux analysis of FSST facilitates understanding of the atmospheric processes responsible for the SST pattern change (Fig. 12b). We use the FOM climatology in the denominator when applying Eq. (6) to FSST to clearly
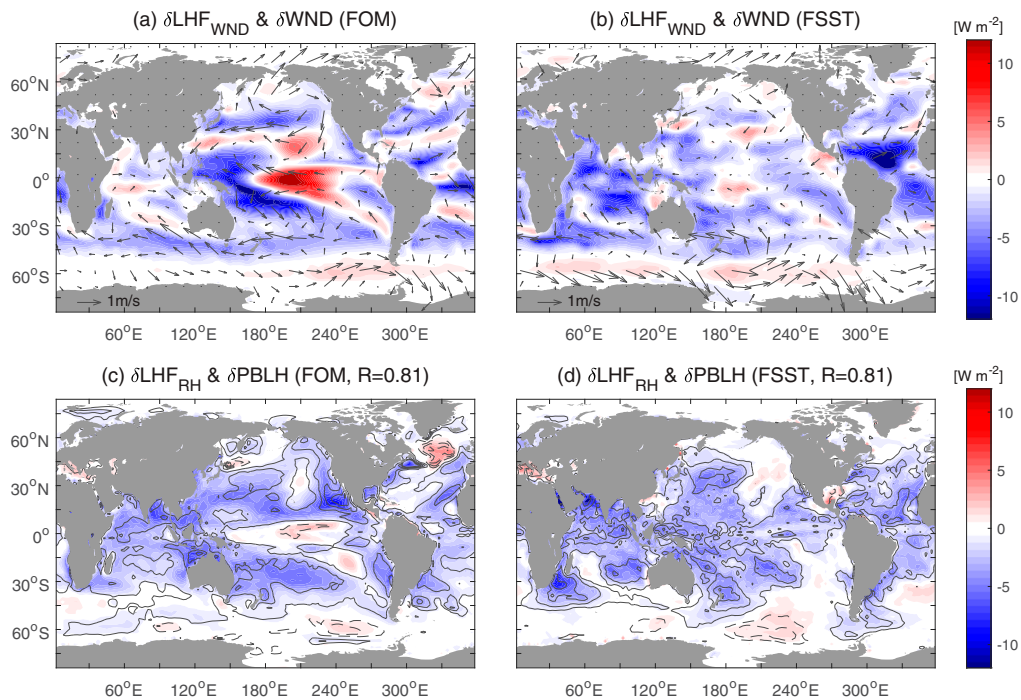

FIG. 11. The difference between k120 and k60 in (a),(b) latent heat flux due to the change in surface wind speed $\delta\mathrm{LHF_{WND}}$ (shading) and surface wind (vectors) and (c),(d) the latent heat flux due to the change in reference-level relative humidity $\delta\mathrm{LHF_{RH}}$ (shading) and the planetary boundary layer (PBL) height (negative in solid and positive in dashed; interval = 15 m). The PBL height is derived from the inversion strength and the near-surface wind speed based on the bulk Richardson method. The pattern correlation coefficient between $\delta\mathrm{LHF_{RH}}$ and the PBL height response is inserted in the title. Results are for FOM in (a) and (c) and FSST in (b) and (d).
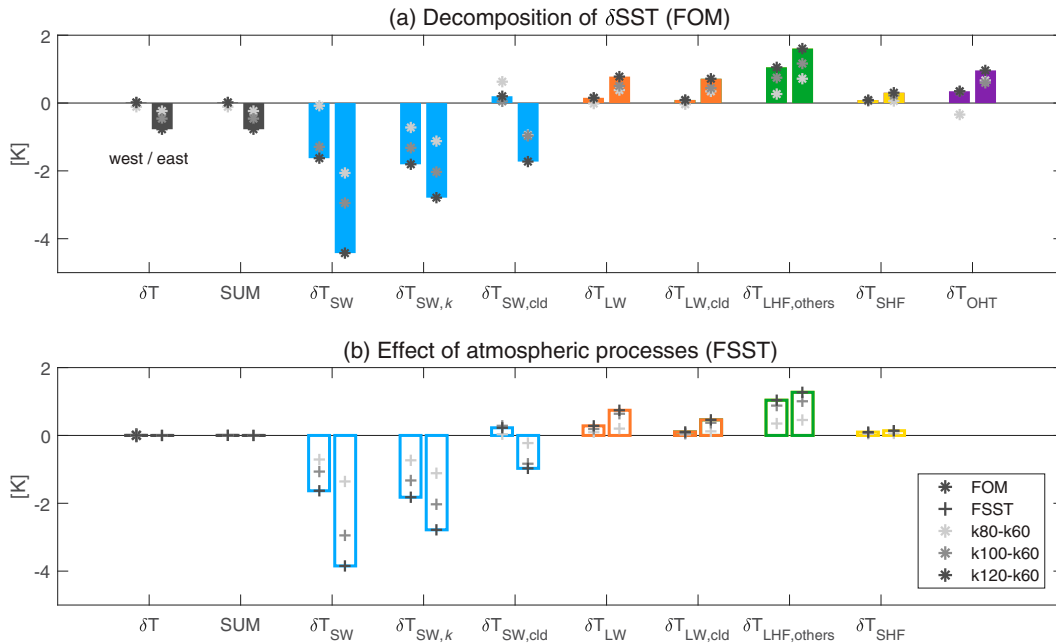
FIG. 12. The decomposition of the SST responses in the western (120–160°E) and eastern (230°–270°E) equatorial (5°S–5°N) Pacific to the components related to surface flux responses in (a) FOM and (b) FSST. Left (right) bar of each pair corresponds to the western (eastern) equatorial Pacific, marked by black rectangles in Fig. 6b. The δT is the actual model response, and SUM is the summation of all components. The detailed description for each component is provided in section 3e.

highlight the effect of surface flux responses. Note that the results are similar to using the FSST climatology. Even with the fixed SSTs, both $\delta T_{SW,k}$ and $\delta T_{SW,cld}$ exhibit a zonal asymmetry comparable to those in FOM, implying that those changes originate from the atmosphere. Since the SW surface forcing is largely zonally uniform over the tropical Pacific (Fig. 5b), the only possible way for $\delta T_{SW,k}$ to exhibit a zonal asymmetry is through the denominator in Eq. (6), $\beta\overline{LHF}$, representing the evaporative damping efficiency (section 2c). The evaporative damping efficiency is weaker in the climatologically colder eastern equatorial Pacific than in the climatologically warmer western equatorial Pacific (Zhang and Li 2014). Therefore, the same magnitude of SW forcing translates into a stronger SST response over the eastern than the western equatorial Pacific.

Also, $\delta T_{SW,cld}$ causes a strong cooling in the eastern equatorial Pacific even with fixed SSTs (Fig. 12b), in response to localized increase in low cloud (Fig. 13b). In CAM4, nonconvective clouds—layered and low-level marine stratus clouds—are parameterized in terms of the relative humidity and/or the lower-tropospheric stability (Neale et al. 2010). Hence, the increase in low cloud amount over the eastern equatorial Pacific can be explained by the increase in lower-tropospheric relative humidity (Fig. 13f), which arises from more specific humidity being trapped in the lower troposphere and is associated with a shrinking of the PBL. The PBL height is lowered due to a larger SW heating rate increase in the lower troposphere (Fig. 13d), as the SW heating rate changes in proportion to its climatological magnitude.

The increase in lower-tropospheric stability, inferred from the change in potential temperature (Fig. 13h), can also lead to increased low cloud. The eastern equatorial Pacific exhibits a larger low cloud increase in FOM than in FSST (cf. Figs. 13a,b), indicating that the dynamical feedback associated with the stronger Walker circulation acts to further lower the PBL and increase the lower tropospheric stability. The cooled eastern equatorial Pacific strengthens the zonal SST gradient across the equatorial Pacific, enhancing the surface easterlies over the central Pacific, and thereby further propagating the cooling westward to form an overall La Niña–like cooling pattern.

4. Implications for the spread among CMIP models

Our water vapor SW absorptivity experiments imply that all else being equal, the climate models with a higher water vapor SW absorptivity would have less global-mean precipitation and a more La Niña–like SST pattern over the tropical Pacific. In this section, we evaluate how our experimental results can be applied to explain the mean-state differences among CMIP5/6 models (Fig. 14).

We first examine whether the intermodel spread of global-mean precipitation can be explained by global-mean SWA. Unlike our CESM experiments, the CMIP5/6 models do not show any significant relationship between global-mean precipitation and SWA (Fig. 14a). Further analysis of the global-mean energy budget reveals that the global-mean precipitation has a significant correlation with LWA in CMIP5 and
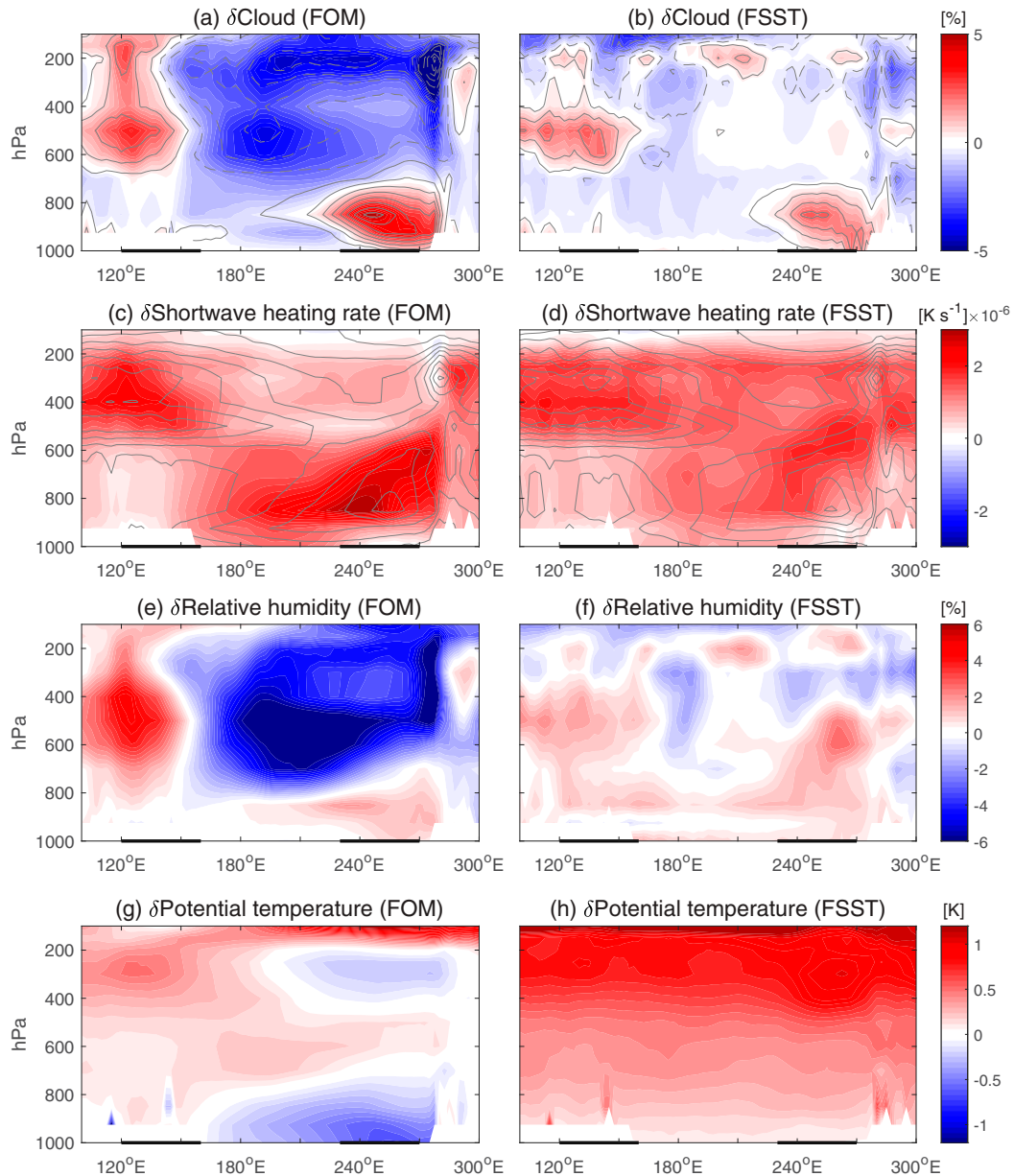
FIG. 13. The difference between k120 and k60 in the equatorial (5°S–5°N) vertical profile of (a),(b) cloud area fraction, (c),(d) atmospheric SW heating rate, (e),(f) relative humidity, and (g),(h) potential temperature in (left) FOM and (right) FSST. The contours in (a) and (b) are the nonconvective cloud responses (interval = 0.8%). The contours in (c) and (d) are the climatological profile of the atmospheric SW heating rate (interval = 1.5×10^{-6} K s^{-1}). The eastern (230°–270°E) and western (120°–160°E) equatorial Pacific are marked by black lines on the horizontal axis.

SHF in CMIP6 (Fig. S4). In addition, the intermodel standard deviation of SWA is the smallest among all atmospheric energy components, amounting to only half that of LWA (Fig. S4). Thus, for the preindustrial mean state of CMIP ensemble, the intermodel spread of global-mean precipitation is dominated by factors other than the SWA intermodel spread.

We next examine whether the intermodel spread in the spatial pattern of equatorial Pacific SST is related to global-mean

SWA. As in our CESM experiments, the CMIP5/6 models with a larger global-mean SWA tend to exhibit a larger zonal SST contrast along the equatorial Pacific (ΔSST_{EW}), defined as the SST difference between the eastern (230°–270°E) and the western (120°–160°E) equatorial (5°S–5°N) Pacific (Fig. 14b). This is also confirmed by regression of equatorial Pacific SST onto global-mean SWA (gray in Figs. 15a,b). To examine whether the same mechanism is at play in the CESM experiments and CMIP5/6, we quantify the contribution of each surface flux
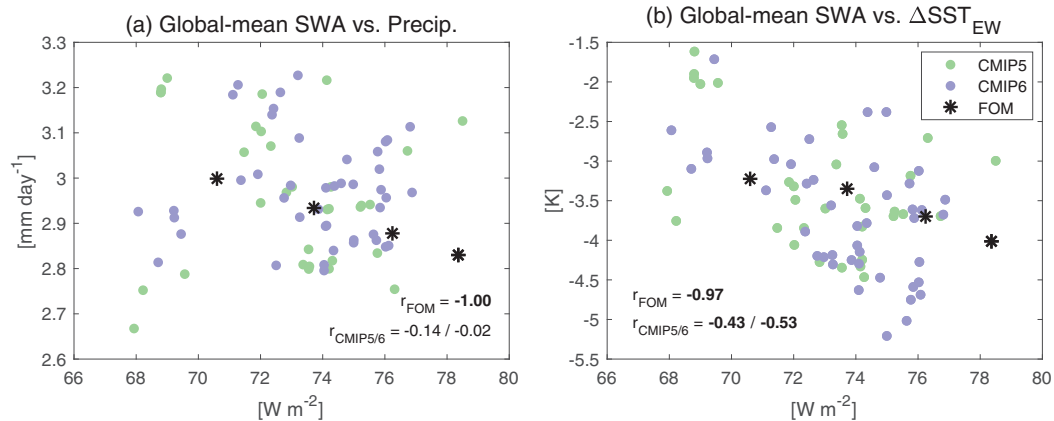
FIG. 14. The scatterplots between the global-mean SWA and (a) global-mean precipitation and (b) zonal asymmetry of the SST between the eastern (230°–270°E) and western (120°–160°E) equatorial (5°S–5°N) Pacific. Green (blue) circles denote the preindustrial simulation of CMIP5 (CMIP6). The FOM experiments with varying water vapor shortwave absorptivity are represented by asterisks. The correlation coefficient is calculated respectively for FOM and CMIP5/6, of which the statistically significant value at the 95% confidence level using a *t* test is inserted as bold text.

component to the intermodel spread in SST pattern using Eq. (6). The multimodel mean is used for the reference climatology in Eq. (6) and δ denotes the deviation from the multimodel mean. For each component, the area average for the tropical Pacific (20°S–20°N, 100°–270°E) is subtracted to highlight the spatial pattern, denoted by an asterisk.

The equatorial Pacific SST pattern (SST^*) associated with each surface flux component is regressed onto the global-mean SWA among the preindustrial simulations of CMIP5 and CMIP6 models (Figs. 15a,b). Only the relevant SW components are displayed, with statistically significant results in bold. In both CMIP5 and CMIP6, higher global-mean SWA is associated with a cooler eastern equatorial Pacific due to the SW cloud effect ($SST^*_{SW,cld}$) (blue dashed lines in Figs. 15a,b) but the relationship in CMIP5 is insignificant at the 95% confidence level. The cooling signal of $SST^*_{SW,cld}$ over the eastern equatorial Pacific is consistent with our CESM experiments, in which the SWA increase leads to the eastern Pacific low cloud enhancement. In addition, the clear-sky SW absorptivity ($SST^*_{SW,\mu_{clr}}$) contributes to cooling over the eastern equatorial Pacific with increasing global-mean SWA (blue dotted lines in Figs. 15a,b). As addressed in section 3a, spread in the clear-sky SW absorptivity induces spread of SW fluxes that is largely zonally uniform over the tropical Pacific (Fig. 3a). However, the zonal contrast in the evaporative damping efficiency results in a stronger cooling by $SST^*_{SW,\mu_{clr}}$ over the eastern than the western basin, as in our CESM experiments.

To recap, the models with a higher global-mean SWA exhibit a stronger cooling by SST^*_{SW} over the eastern equatorial Pacific in the preindustrial simulations of both CMIP5 and CMIP6, mostly resulting from $SST^*_{SW,cld}$, with a smaller contribution from $SST^*_{SW,\mu_{clr}}$ (Figs. 15a,b and Fig. S5). An analogous regression analysis with the AMIP simulations (Figs. 15a,b and Fig. S5) suggests that the intermodel relationships regarding $SST^*_{SW,cld}$ and $SST^*_{SW,\mu_{clr}}$ largely arise from the intermodel differences in atmospheric rather than oceanic or

coupled processes. The dominance of atmospheric processes further ensures that $SST^*_{SW,\mu_{clr}}$ and $SST^*_{SW,cld}$ signals congruent with the global-mean SWA in the CMIP5/6 originate from mechanisms common to our CESM experiments (cf. the CMIP ensemble and the CESM experiment results in Figs. S5b,c), although the CMIP intermodel range in $SST^*_{SW,cld}$ over the eastern equatorial Pacific is 4 times as large as the range produced by varying the water vapor SW absorptivity in CESM (Fig. S5b). This indicates that the uncertainties unrelated to the SWA intermodel spread could be responsible for a large fraction of the intermodel difference in low clouds.

We now compare the effect of SWA intermodel spread with the effect of other processes in creating the zonal SST asymmetry in the equatorial Pacific. For this purpose, the equatorial Pacific SST^* related to the individual surface flux components are regressed onto ΔSST_{EW} (Figs. 15c,d). In CMIP5, a strong cooling over the eastern equatorial Pacific by ocean heat transport (SST^*_{OHT}) is most responsible for a large ΔSST_{EW} (Fig. 15c). This is consistent with previous studies that emphasize the uncertainty in ocean dynamics for introducing the intermodel spread in the tropical Pacific SST pattern (Zheng et al. 2012; Li et al. 2015; Burls et al. 2017). In CMIP6, on the other hand, the SW cloud effect ($SST^*_{SW,cld}$) is most responsible for cooling over the eastern equatorial Pacific, with a weak contribution from SST^*_{OHT} (Fig. 15d). This implies an importance of the SWA intermodel spread for the uncertainty of tropical Pacific SST pattern among CMIP6 models, because the intermodel spread of $SST^*_{SW,cld}$ over the eastern basin is congruent with the SWA intermodel spread (Fig. 15b and Fig. S5b). As the SW cloud effect increases the east–west contrast in the equatorial Pacific SST, the easterly trade winds strengthen and consequently the non-SST-related evaporation ($SST^*_{LHF,others}$) induces a cooling signal extending from the eastern to the central Pacific (Fig. 15d). Hence this $SST^*_{LHF,others}$ signal acts to amplify the zonal asymmetry associated with $SST^*_{SW,cld}$.
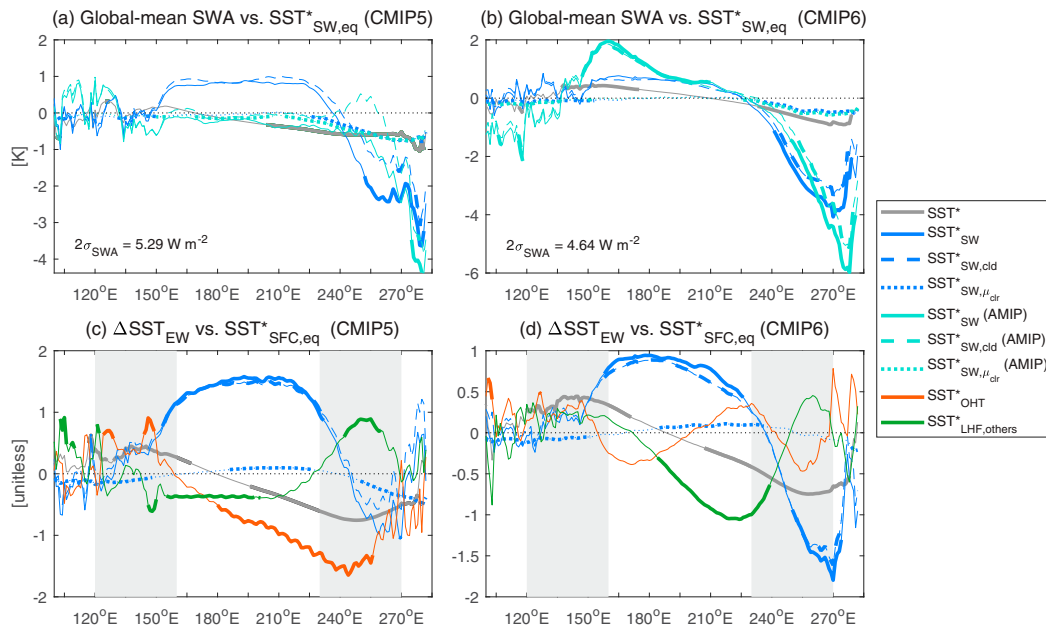
FIG. 15. The intermodel regression of equatorial (5°S–5°N) SST pattern (SST*) onto the global-mean SWA in (a) CMIP5 and (b) CMIP6 preindustrial simulations. The regression line for the actual SST* is plotted in a gray line and that for SST* induced by the surface SW fluxes in blue. The intermodel regression of the SST* induced by AMIP SW fluxes onto the global-mean SWA is denoted as cyan lines, where the available 19 (30) subsets of CMIP5 (CMIP6) models are used. Note that the regression coefficients are multiplied by two intermodel standard deviations of global-mean SWA ($2\sigma_{SWA}$), of which the magnitude is inserted in the lower left corner. The intermodel regression of SST* induced by each surface flux component onto the zonal asymmetry in SST (ΔSST_{EW}) in (c) CMIP5 and (d) CMIP6. The description for each component is provided in section 4. The eastern (230°–270°E) and western (120°–160°E) equatorial Pacific used for calculating ΔSST_{EW} are shaded in gray. Note that the statistically significant regression values according to the t test at the 95% confidence level are in thicker lines.

5. Summary and conclusions

In this study, we investigate the effect of SWA intermodel spread on the mean climate state. First, the large intermodel spread of global-mean SWA in CMIP models is shown to be primarily due to the uncertainty in water vapor SW absorptivity through an analysis combining the APRP method and radiative kernel technique. To isolate the effect of the SWA intermodel spread on the preindustrial climate simulations, we carry out model experiments where the water vapor SW absorptivity is altered in the radiative transfer code of CESM1.2.2 with CAM4 atmospheric physics. Our CESM experiments reveal that an increase in the water vapor SW absorptivity induces 1) a significant global-mean precipitation reduction (Fig. 6a) and 2) a La Niña–like cooling pattern over the tropical Pacific (Fig. 6b).

The global-mean precipitation change is analyzed in the framework of the atmospheric energy budget. Higher water vapor SW absorptivity increases the global-mean SWA, which is partially compensated by the reduction in SW absorption by clouds. The SWA increase heats the atmosphere and cools the surface, enhancing atmospheric LW cooling. The resulting increase in atmospheric stability shifts cloud water from the upper to the lower troposphere, further enhancing the LW compensation. As a result, the radiative cooling and the SHF reduction compensate about half of the SWA increase

induced by the increase in water vapor SW absorptivity, leaving the other half to be compensated by a reduction of precipitation (and evaporation).

We undertake a complementary exploration of the mechanisms responsible for the evaporation reduction by decomposing the bulk flux formula at the surface. As the increase in water vapor SW absorptivity stabilizes the atmosphere, the Hadley circulation weakens and the midlatitude jet shifts poleward, leading to a weakening of surface winds, thereby reducing the evaporation. A shallower PBL associated with a more stable atmosphere also acts to reduce the evaporation. Moreover, higher SWA cools the surface and the resulting decrease in saturation vapor pressure at the ocean surface contributes further evaporation reduction. The net evaporation reduction over the ocean surface is strongly coupled to the decreased convective heating in the free atmosphere, effectively compensating the increased SWA aloft.

Even though the SW forcing profile due to altered water vapor SW absorptivity is nearly zonally uniform over the tropical Pacific, the SST decrease is larger in the eastern than the western equatorial Pacific, featuring a La Niña–like cooling pattern. Decomposition of the contributions to SST gradient reveal that this is partly because the evaporative damping efficiency is smaller in the eastern than the western equatorial
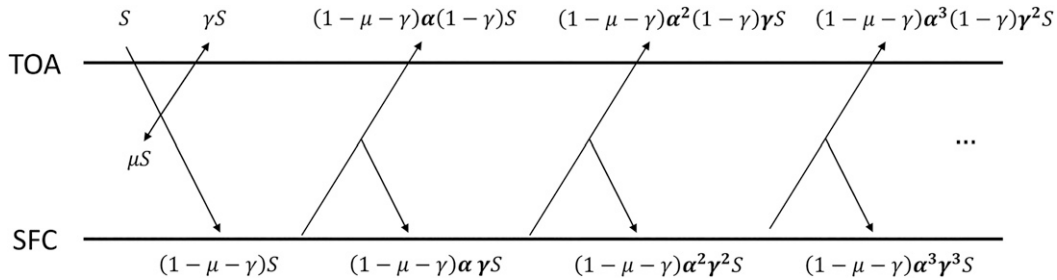
FIG. A1. Schematic of one-layer radiation model used in this study. S, μ, γ, and α indicate the insolation, atmospheric absorptivity, atmospheric reflectivity, and surface albedo; TOA is top of atmosphere; SFC is surface.

Pacific associated with the contrast in the climatological SST. In addition, the enhanced SWA leads to a local increase in low cloud amount over the eastern equatorial Pacific, leading to an enhanced zonal contrast in the equatorial Pacific SST.

We show that the water vapor SW absorptivity experiments with the CESM model have implications for the intermodel uncertainty of the tropical Pacific SST pattern in CMIP multimodel ensemble. The models with a higher global-mean SWA simulate a more La Niña–like mean state over the tropical Pacific. Although the uncertainties in ocean dynamics and/or cloud parameterization are the dominant cause of the intermodel spread of east–west asymmetry in the tropical Pacific SST, the intermodel regression analysis reveals a contribution from the SW cloud effect in CMIP6, which in turn arises from the spread in the water vapor SW absorptivity. To our knowledge, this is the first study to address the SWA impact on the spatial pattern of the tropical Pacific climate. Our results provide valuable insights to the notorious cold tongue biases (Mechoso et al. 1995; Lin 2007; Flato et al. 2013; Stouffer et al. 2017).

Our experiments demonstrate that altered water vapor SW absorptivity can modulate the tropical Pacific SST pattern through changes in cloud radiative effects. It is interesting to note a substantial change in SW cloud effect, despite that the direct effect of an altered water vapor SW absorptivity is on the clear-sky SW fluxes. This suggests an important way in which uncertainties in the parameterization of SW absorption can lead to uncertainties in cloud radiative effects. Our findings reinforce the importance of improving the parameterization of SW absorption (Kelley et al. 2020) for increasing the fidelity of climate models in simulating the mean climate state.

APPENDIX

Extension of the APRP Method

For the APRP method, the one-layer radiation model is adopted to represent the interaction of SW fluxes between the atmosphere and surface (Fig. A1). Of the incident solar radiation S, a fraction μ is absorbed by the atmosphere, a fraction γ is reflected by the atmosphere, and the remainder is transmitted to the surface. Of the solar radiation transmitted through the atmosphere, a fraction α is reflected at the surface, of which a fraction γ is reflected from the atmosphere back toward the surface again on the return pass. This is repeated for infinite passes. Note that the atmospheric absorption and reflection occur simultaneously at the first downward pass motivated by Donohoe and Battisti (2011).

In this one-layer radiation model, the total reflected SW radiation at TOA ($SW_\uparrow^{TOA}$) and total incident SW radiation toward SFC ($SW_\downarrow^{SFC}$) can be expressed as the sum of an infinite geometric series, with $\alpha\gamma$ as the common ratio. Then, the planetary albedo (A) and surface incident ratio (Q_s) are expressed as a function of radiative properties:

$$
\begin{aligned}
A(\alpha, \gamma, \mu) &= \frac{SW_\uparrow^{TOA}}{S} \\
&= \gamma + (1 - \mu - \gamma)(1 - \gamma)\alpha(1 + \alpha\gamma + \alpha^2\gamma^2 + \cdots) \\
&= \gamma + \frac{(1 - \mu - \gamma)(1 - \gamma)}{1 - \alpha\gamma}\alpha,
\end{aligned}
\tag{A1}
$$

$$Q_s(\alpha, \gamma, \mu) = \frac{\mathrm{SW}_\downarrow^{\mathrm{SFC}}}{S} = (1 - \mu - \gamma)(1 + \alpha\gamma + \alpha^2\gamma^2 + \cdots)$$

$$= \frac{(1 - \mu - \gamma)}{1 - \alpha\gamma} . \tag{A2}$$

To account for the effect of clouds, all-sky radiative fluxes at each grid point (R) are divided into the clear-sky (R_{clr}) and overcast-sky (R_{oc}) fluxes, weighted by the total-column cloud area fraction (clt) following Taylor et al. (2007):

$$R = (1 - \mathrm{clt}) \times R_{\mathrm{clr}} + \mathrm{clt} \times R_{\mathrm{oc}}. \tag{A3}$$

Note that R_{oc} can be calculated from the standard model outputs R, R_{clr}, and clt. The one-layer radiation model is applied to each of R_{clr} and R_{oc}. Accordingly, radiative properties for the single-column model are calculated for clear- and overcast-sky fluxes:

$$A = \frac{\mathrm{SW}_\uparrow^{\mathrm{TOA}}}{S}, \quad Q_s = \frac{\mathrm{SW}_\downarrow^{\mathrm{SFC}}}{S}, \quad \alpha = \frac{\mathrm{SW}_\uparrow^{\mathrm{SFC}}}{\mathrm{SW}_\downarrow^{\mathrm{SFC}}}. \tag{A4}$$

The atmospheric absorptivity is defined as the difference between the fraction of net SW fluxes absorbed at TOA and SFC:

$$\mu = (1 - A) - Q_s(1 - \alpha). \tag{A5}$$

The atmospheric reflectivity is then derived from Eq. (A2):

$$\gamma = \frac{1 - \mu - Q_s}{1 - \alpha Q_s}. \tag{A6}$$

In Eqs. (A3)–(A6), the radiative properties for clear-sky (α_{clr}, μ_{clr}, γ_{clr}) and overcast-sky (α_{oc}, μ_{oc}, γ_{oc}) are fitted to the climate model output. Radiative properties for the overcast-sky are calculated assuming that the non-cloud atmospheric constituents in the overcast-sky absorb and reflect the same amount of SW fluxes as in the clear-sky. That is, the transmittance in overcast-sky is the product of transmittance in clear-sky and cloud, applied to μ and γ in the same way:

$$\begin{aligned} 1 - \mu_{\mathrm{oc}} &= (1 - \mu_{\mathrm{clr}}) \times (1 - \mu_{\mathrm{cld}}), \\ 1 - \gamma_{\mathrm{oc}} &= (1 - \gamma_{\mathrm{clr}}) \times (1 - \gamma_{\mathrm{cld}}). \end{aligned} \tag{A7}$$

This results in seven radiative properties (clt, α_{clr}, α_{oc}, μ_{clr}, μ_{cld}, γ_{clr}, γ_{cld}) representing the SW radiative transfer in the climate model. Next, we extend the methodology for TOA SW decomposition in the original APRP method (Taylor et al. 2007) to the surface component in a parallel way. First, A [Eq. (A1)] and Q_s [Eq. (A2)] of the climate model become a function of the seven radiative properties:

$$A_{\mathrm{clr}}(\alpha_{\mathrm{clr}}, \gamma_{\mathrm{clr}}, \mu_{\mathrm{clr}}) = \gamma_{\mathrm{clr}} + \frac{(1 - \mu_{\mathrm{clr}} - \gamma_{\mathrm{clr}})(1 - \gamma_{\mathrm{clr}})}{1 - \alpha_{\mathrm{clr}}\gamma_{\mathrm{clr}}}\alpha_{\mathrm{clr}}, \tag{A8}$$

$$A_{\mathrm{oc}}(\alpha_{\mathrm{oc}}, \gamma_{\mathrm{old}}, \mu_{\mathrm{cla}}, \gamma_{\mathrm{clr}}, \mu_{\mathrm{clr}})$$

$$= \gamma_{\mathrm{oc}} + \frac{(1 - \mu_{\mathrm{oc}} - \gamma_{\mathrm{oc}})(1 - \gamma_{\mathrm{oc}})}{1 - a_{\mathrm{nn}}\gamma_{\mathrm{nf}}}\alpha_{\mathrm{oc}}, \text{ where}$$

$$\begin{aligned} \mu_{\mathrm{oc}} &= 1 - (1 - \mu_{\mathrm{clr}}) \times (1 - \mu_{\mathrm{cld}}), \\ \gamma_{\mathrm{oc}} &= 1 - (1 - \gamma_{\mathrm{clr}}) \times (1 - \gamma_{\mathrm{cld}}), \end{aligned} \tag{A9}$$

$$A(\mathrm{clt}, \alpha_{\mathrm{clr}}, \alpha_{\mathrm{oc}}, \mu_{\mathrm{clr}}, \mu_{\mathrm{cld}}, \gamma_{\mathrm{clr}}, \gamma_{\mathrm{cld}}) = (1 - \mathrm{clt}) \times A_{\mathrm{clr}}$$

$$+ \mathrm{clt} \times A_{\mathrm{oc}}, \tag{A10}$$

$$Q_{s,\mathrm{clr}}(\alpha_{\mathrm{clr}}, \gamma_{\mathrm{clr}}, \mu_{\mathrm{clr}}) = \frac{(1 - \mu_{\mathrm{clr}} - \gamma_{\mathrm{clr}})}{1 - \alpha_{\mathrm{clr}}\gamma_{\mathrm{clr}}}, \tag{A11}$$

$$Q_{s,\mathrm{oc}}(\alpha_{\mathrm{oc}}, \gamma_{\mathrm{cld}}, \mu_{\mathrm{cld}}, \gamma_{\mathrm{clr}}, \mu_{\mathrm{clr}}) = \frac{(1 - \mu_{\mathrm{oc}} - \gamma_{\mathrm{oc}})}{1 - \alpha_{\mathrm{oc}}\gamma_{\mathrm{oc}}}, \text{ where}$$

$$\begin{aligned} \mu_{\mathrm{oc}} &= 1 - (1 - \mu_{\mathrm{clr}}) \times (1 - \mu_{\mathrm{cld}}), \\ \gamma_{\mathrm{oc}} &= 1 - (1 - \gamma_{\mathrm{clr}}) \times (1 - \gamma_{\mathrm{cld}}), \text{ and} \end{aligned} \tag{A12}$$

$$Q_s(\mathrm{clt}, \alpha_{\mathrm{clr}}, \alpha_{\mathrm{oc}}, \mu_{\mathrm{clr}}, \mu_{\mathrm{cld}}, \gamma_{\mathrm{clr}}, \gamma_{\mathrm{cld}}) = (1 - \mathrm{clt})$$

$$\times Q_{s,\mathrm{clr}} + \mathrm{clt} \times Q_{s,\mathrm{oc}}. \tag{A13}$$

The changes in planetary albedo (δA) and surface incident ratio (δQ_s) due to each radiative property can be estimated by Eqs. (A10) and (A13). The forward and backward substitution are averaged to estimate a contribution from each radiative property, following Colman (2003):

$$\delta A_t = \frac{1}{2}[A(t_2, o_1) - A(t_1, o_1)] + \frac{1}{2}[A(t_2, o_2) - A(t_1, o_2)], \tag{A14}$$

$$\delta Q_{s,t} = \frac{1}{2}[Q_s(t_2, o_1) - Q_s(t_1, o_1)]$$

$$+ \frac{1}{2}[Q_s(t_2, o_2) - Q_s(t_1, o_2)], \tag{A15}$$

where t denotes target radiative property, o denotes all other six radiative properties, and δ denotes the difference between state 1 and state 2.

Meanwhile, the net SW flux at the TOA and SFC are

$$\mathrm{SW}_{\mathrm{net}}^{\mathrm{TOA}} = S - \mathrm{SW}_\uparrow^{\mathrm{TOA}} = (1 - A)S, \text{ and} \tag{A16}$$

$$\mathrm{SW}_{\mathrm{net}}^{\mathrm{SFC}} = \mathrm{SW}_\downarrow^{\mathrm{SFC}} - \mathrm{SW}_\uparrow^{\mathrm{SFC}} = Q_s(1 - \alpha)S, \tag{A17}$$

and the changes in SW flux at the TOA and SFC are

$$\delta\mathrm{SW}_{\mathrm{net}}^{\mathrm{TOA}} = \delta[(1 - A)S] = (1 - A)\delta S - S\delta A \text{ and} \tag{A18}$$

$$\delta\mathrm{SW}_{\mathrm{net}}^{\mathrm{SFC}} = \delta[Q_s(1 - \alpha)S]$$

$$= Q_s(1 - \alpha)\delta S - Q_s S\delta\alpha + (1 - \alpha)S\delta Q_s, \tag{A19}$$

where the terms without δ are the average between the two states, and the covariance terms are ignored.

Substituting Eq. (A14) into (A18) and Eq. (A15) into (A19), SW flux responses at the TOA and SFC can be attributed to the change in each radiative property:

$$\delta SW_{net}^{TOA} = (1 - A)\delta S - S[\delta A_{\alpha_{clr}} + \delta A_{\alpha_{oc}}] \cdots$$
$$- S[\delta A_{clt} + \delta A_{\mu_{cld}} + \delta A_{\gamma_{cld}}]$$
$$- S[\delta A_{\gamma_{cir}} + \delta A_{\mu_{clr}}]$$
$$= \delta SW_S^{TOA} + \delta SW_\alpha^{TOA} + \delta SW_{cld}^{TOA} + \delta SW_{ncld}^{TOA}$$
$$(A20)$$

$$\delta SW_{net}^{SFC} = Q_s(1 - \alpha)\delta S$$
$$+ [-Q_s S\delta\alpha + S(1 - \alpha)(\delta Q_{s,\alpha_{clr}} + \delta Q_{s,\alpha_{oc}})]\cdots$$
$$+ S(1 - \alpha)(\delta Q_{s,clt} + \delta Q_{s,\mu_{cld}} + \delta Q_{s,\gamma_{cld}})$$
$$+ S(1 - \alpha)(\delta Q_{s,\mu_{clr}} + \delta Q_{s,\gamma_{clr}})$$
$$= \delta SW_S^{SFC} + \delta SW_\alpha^{SFC} + \delta SW_{cld}^{SFC} + \delta SW_{ncld}^{SFC},$$
$$(A21)$$

where subscripts S, α, cld, and ncld denote the contributions from the change in insolation, surface albedo, cloud properties, and non-cloud atmospheric constituents, respectively.

REFERENCES

Allen, M., and W. Ingram, 2002: Constraints on future changes in climate and the hydrologic cycle. *Nature*, **419**, 228–232, https://doi.org/10.1038/nature01092.

Arking, A., 1996: Absorption of solar energy in the atmosphere: Discrepancy between model and observations. *Science*, **273**, 779–782, https://doi.org/10.1126/science.273.5276.779.

Burls, N. J., L. Muir, E. M. Vincent, and A. Fedorov, 2017: Extratropical origin of equatorial Pacific cold bias in climate models with links to cloud albedo. *Climate Dyn.*, **49**, 2093–2113, https://doi.org/10.1007/s00382-016-3435-6.

Collins, W. D., J. M. Lee-Taylor, D. P. Edwards, and G. L. Francis, 2006: Effects of increased near-infrared absorption by water vapor on the climate system. *J. Geophys. Res.*, **111**, D18109, https://doi.org/10.1029/2005JD006796.

Colman, R., 2003: A comparison of climate feedbacks in general circulation models. *Climate Dyn.*, **20**, 865–873, https://doi.org/10.1007/s00382-003-0310-z.

DeAngelis, A. M., X. Qu, M. D. Zelinka, and A. Hall, 2015: An observational radiative constraint on hydrologic cycle intensification. *Nature*, **528**, 249–253, https://doi.org/10.1038/nature15770.

Donohoe, A., and D. S. Battisti, 2011: Atmospheric and surface contributions to planetary albedo. *J. Climate*, **24**, 4402–4418, https://doi.org/10.1175/2011JCLI3946.1.

Eyring, V., S. Bony, G. A. Meehl, C. A. Senior, B. Stevens, R. J. Stouffer, and K. E. Taylor, 2016: Overview of the Coupled Model Intercomparison Project Phase 6 (CMIP6) experimental design and organization. *Geosci. Model Dev.*, **9**, 1937–1958, https://doi.org/10.5194/gmd-9-1937-2016.

Fiedler, S., and Coauthors, 2019: Anthropogenic aerosol forcing-insights from multiple estimates from aerosol–climate models

with reduced complexity. *Atmos. Chem. Phys.*, **19**, 6821–6841, https://doi.org/10.5194/acp-19-6821-2019.

Fläschner, D., T. Mauritsen, and B. Stevens, 2016: Understanding the intermodel spread in global-mean hydrological sensitivity. *J. Climate*, **29**, 801–817, https://doi.org/10.1175/JCLI-D-15-0351.1.

Flato, G., and Coauthors, 2013: Evaluation of climate models. *Climate Change 2013: The Physical Science Basis*, T. F. Stocker et al., Eds., Cambridge University Press, 741–866.

Freidenreich, S. M., and V. Ramaswamy, 1999: A new multiple-band solar radiative parameterization for general circulation models. *J. Geophys. Res.*, **104**, 31 389–31 409, https://doi.org/10.1029/1999JD900456.

Frey, W. R., E. A. Maroon, A. G. Pendergrass, and J. E. Kay, 2017: Do Southern Ocean cloud feedbacks matter for 21st century warming? *Geophys. Res. Lett.*, **44**, 12 447–12 456, https://doi.org/10.1002/2017GL076339.

Gent, P. R., and Coauthors, 2011: The Community Climate System Model version 4. *J. Climate*, **24**, 4973–4991, https://doi.org/10.1175/2011JCLI4083.1.

Hunke, E. C., and W. H. Lipscomb, 2008: CICE: The Los Alamos sea ice model user's manual, version 4. Los Alamos National Laboratory Tech. Rep. LA-CC-06-012, 72 pp., https://www.researchgate.net/publication/237249046_CICE_The_Los_Alamos_sea_ice_model_documentation_and_software_user's_manual_version_40_LA-CC-06-012.

Hurrell, J. W., J. J. Hack, D. Shea, J. M. Caron, and J. Rosinski, 2008: A new sea surface temperature and sea ice boundary dataset for the Community Atmosphere Model. *J. Climate*, **21**, 5145–5153, https://doi.org/10.1175/2008JCLI2292.1.

Hwang, Y. T., D. M. W. Frierson, and S. M. Kang, 2013: Anthropogenic sulfate aerosol and the southward shift of tropical precipitation in the late 20th century. *Geophys. Res. Lett.*, **40**, 2845–2850, https://doi.org/10.1002/grl.50502.

Jia, F., and L. Wu, 2013: A study of response of the equatorial Pacific SST to doubled-CO_2 forcing in the coupled CAM–1.5-layer reduced-gravity ocean model. *J. Phys. Oceanogr.*, **43**, 1288–1300, https://doi.org/10.1175/JPO-D-12-0144.1.

Kelley, M., and Coauthors, 2020: GISS-E2.1: Configurations and climatology. *J. Adv. Model. Earth Syst.*, **12**, e2019MS002025, https://doi.org/10.1029/2019MS002025.

Kiehl, J. T., and K. E. Trenberth, 1997: Earth's annual global mean energy budget. *Bull. Amer. Meteor. Soc.*, **78**, 197–208, https://doi.org/10.1175/1520-0477(1997)078<0197:EAGMEB>2.0.CO;2.

——, J. J. Hack, M. H. Zhang, and R. D. Cess, 1995: Sensitivity of a GCM climate to enhanced shortwave cloud absorption. *J. Climate*, **8**, 2200–2212, https://doi.org/10.1175/1520-0442(1995)008<2200:SOAGCT>2.0.CO;2.

Kim, D., and V. Ramanathan, 2008: Solar radiation budget and radiative forcing due to aerosols and clouds. *J. Geophys. Res.*, **113**, https://doi.org/10.1029/2007JD008434.

Lawrence, D. M., and Coauthors, 2011: Parameterization improvements and functional and structural advances in version 4 of the Community Land Model. *J. Adv. Model. Earth Syst.*, **3**, 27 pp., https://doi.org/10.1029/2011MS000045.

Li, G., Y. Du, H. Xu, and B. Ren, 2015: An intermodel approach to identify the source of excessive equatorial Pacific cold tongue in CMIP5 models and uncertainty in observational datasets. *J. Climate*, **28**, 7630–7640, https://doi.org/10.1175/JCLI-D-15-0168.1.

Lin, J. L., 2007: The double-ITCZ problem in IPCC AR4 coupled GCMs: Ocean–atmosphere feedback analysis. *J. Climate*, **20**, 4497–4525, https://doi.org/10.1175/JCLI4272.1.

Lohmann, U., and R. Bennartz, 2002: Impact of improved near-infrared water vapor line data in simulations with the ECHAM4 general circulation model. *J. Geophys. Res.*, **107**, 4288, https://doi.org/10.1029/2001JD001101.

Lu, J., G. A. Vecchi, and T. Reichler, 2007: Expansion of the Hadley cell under global warming. Geophys. *Res. Lett.*, **34**, L06805, https://doi.org/10.1029/2006GL028443.

Mechoso, C. R., and Coauthors, 1995: The seasonal cycle over the tropical Pacific in coupled ocean–atmosphere general circulation models. *Mon. Wea. Rev.*, **123**, 2825–2838, https://doi.org/10.1175/1520-0493(1995)123<2825:TSCOTT>2.0.CO;2.

Neale, R. B., and Coauthors, 2010: Description of the NCAR Community Atmosphere Model (CAM 4.0). NCAR Tech. Note NCAR/TN-485+STR, 212 pp., http://www.cesm.ucar.edu/models/ccsm4.0/cam/docs/description/cam4_desc.pdf.

——, J. Richter, S. Park, P. H. Lauritzen, S. J. Vavrus, P. J. Rasch, and M. Zhang, 2013: The mean climate of the Community Atmosphere Model (CAM4) in forced SST and fully coupled experiments. *J. Climate*, **26**, 5150–5168, https://doi.org/10.1175/JCLI-D-12-00236.1.

O'Gorman, P. A., R. P. Allan, M. P. Byrne, and M. Previdi, 2012: Energetic constraints on precipitation under climate change. *Surv. Geophys.*, **33**, 585–608, https://doi.org/10.1007/s10712-011-9159-6.

Paynter, D., and V. Ramaswamy, 2014: Investigating the impact of the shortwave water vapor continuum upon climate simulations using GFDL global models. *J. Geophys. Res. Atmos.*, **119**, 10 720–10 737, https://doi.org/10.1002/2014JD021881.

Pendergrass, A. G., 2020: The global-mean precipitation response to CO_2-induced warming in CMIP6 models. *Geophys. Res. Lett.*, **47**, e2020GL089964, https://doi.org/10.1029/2020GL089964.

——, A. Conley, and F. M. Vitt, 2018: Surface and top-of-atmosphere radiative feedback kernels for CESM-CAM5. *Earth Syst. Sci. Data*, **10**, 317–324, https://doi.org/10.5194/essd-10-317-2018.

Pincus, R., and Coauthors, 2015: Radiative flux and forcing parameterization error in aerosol-free clear skies. *Geophys. Res. Lett.*, **42**, 5485–5492, https://doi.org/10.1002/2015GL064291.

Previdi, M., 2010: Radiative feedbacks on global precipitation. *Environ. Res. Lett.*, **5**, 025211, https://doi.org/10.1088/1748-9326/5/2/025211.

Smith, R. D., and Coauthors, 2010: The Parallel Ocean Program (POP) reference manual. Los Alamos National Laboratory Tech. Rep. LAUR-10-01853, 140 pp., https://www.cesm.ucar.edu/models/cesm1.0/pop2/doc/sci/POPRefManual.pdf.

Soden, B. J., and I. M. Held, 2006: An assessment of climate feedbacks in coupled ocean–atmosphere models. *J. Climate*, **19**, 3354–3360, https://doi.org/10.1175/JCLI3799.1.

——, ——, R. Colman, K. M. Shell, J. T. Kiehl, and C. A. Shields, 2008: Quantifying climate feedbacks using radiative kernels. *J. Climate*, **21**, 3504–3520, https://doi.org/10.1175/2007JCLI2110.1.

Stouffer, R. J., V. Eyring, G. A. Meehl, S. Bony, C. Senior, B. Stevens, and K. E. Taylor, 2017: CMIP5 scientific gaps and recommendations for CMIP6. *Bull. Amer. Meteor. Soc.*, **98**, 95–105, https://doi.org/10.1175/BAMS-D-15-00013.1.

Takahashi, K., 2009a: Radiative constraints on the hydrological cycle in an idealized radiative–convective equilibrium model. *J. Atmos. Sci.*, **66**, 77–91, https://doi.org/10.1175/2008JAS2797.1.

——, 2009b: The global hydrological cycle and atmospheric shortwave absorption in climate models under CO_2 forcing. *J. Climate*, **22**, 5667–5675, https://doi.org/10.1175/2009JCLI2674.1.

Taylor, K. E., M. Crucifix, P. Braconnot, C. D. Hewitt, C. Doutriaux, A. J. Broccoli, J. F. B. Mitchell, and M. J. Webb, 2007: Estimating shortwave radiative forcing and response in climate models. *J. Climate*, **20**, 2530–2543, https://doi.org/10.1175/JCLI4143.1.

——, R. J. Stouffer, and G. A. Meehl, 2012: An overview of CMIP5 and the experiment design. *Bull. Amer. Meteor. Soc.*, **93**, 485–498, https://doi.org/10.1175/BAMS-D-11-00094.1.

Wild, M., 2008: Short-wave and long-wave surface radiation budgets in GCMs: A review based on the IPCC-AR4/CMIP3 models. *Tellus*, **60A**, 932–945, https://doi.org/10.1111/j.1600-0870.2008.00342.x.

——, 2020: The global energy balance as represented in CMIP6 climate models. *Climate Dyn.*, **55**, 553–577, https://doi.org/10.1007/s00382-020-05282-7.

——, and Coauthors, 2015: The energy balance over land and oceans: An assessment based on direct observations and CMIP5 climate models. *Climate Dyn.*, **44**, 3393–3429, https://doi.org/10.1007/s00382-014-2430-z.

Xie, S.-P., C. Deser, G. A. Vecchi, J. Ma, H. Teng, and A. T. Wittenberg, 2010: Global warming pattern formation: Sea surface temperature and rainfall. *J. Climate*, **23**, 966–986, https://doi.org/10.1175/2009JCLI3329.1.

Yoshimori, M., J. C. Hargreaves, J. D. Annan, T. Yokohata, and A. Abe-Ouchi, 2011: Dependency of feedbacks on forcing and climate state in physics parameter ensembles. *J. Climate*, **24**, 6440–6455, https://doi.org/10.1175/2011JCLI3954.1.

Zelinka, M. D., T. A. Myers, D. T. McCoy, S. Po-Chedley, P. M. Caldwell, P. Ceppi, S. A. Klein, and K. E. Taylor, 2020: Causes of higher climate sensitivity in CMIP6 models. *Geophys. Res. Lett.*, **12**, e2019GL085782, https://doi.org/10.1029/2019GL085782.

Zhang, L., and T. Li, 2014: A simple analytical model for understanding the formation of sea surface temperature patterns under global warming. *J. Climate*, **27**, 8413–8421, https://doi.org/10.1175/JCLI-D-14-00346.1.

Zheng, Y., J. L. Lin, and T. Shinoda, 2012: The equatorial Pacific cold tongue simulated by IPCC AR4 coupled GCMs: Upper ocean heat budget and feedback analysis. *J. Geophys. Res.*, **117**, C05024, https://doi.org/10.1029/2011JC007746.